JGR Space Physics

RESEARCH ARTICLE
10.1029/2020JA028505

Key Points:

- We investigate the variations of the neutral wind and temperature before the Strong Thermal Emission Velocity Enhancement (STEVE) emergence using joint scanning Doppler imager and optical all-sky imager observations
- Winds enhance in westward/southward directions following substorm, but the southward winds feature a stop latitude before STEVE emergence
- The neutral wind may lead to the transport/pileup of neutral constituents at subauroral latitudes and contribute to STEVE airglow production

Supporting Information:

- Supporting Information S1
- Movie S1
- Movie S2
- Movie S3

Correspondence to:
J. Liang,
liangj@ucalgary.ca

Citation:
Liang, J., Zou, Y., Nishimura, Y., Donovan, E., Spanswick, E., & Conde, M. (2021). Neutral wind dynamics preceding the STEVE occurrence and their possible preconditioning role in STEVE formation. *Journal of Geophysical Research: Space Physics*, *126*, e2020JA028505. https://doi.org/10.1029/2020JA028505

Received 21 JUL 2020
Accepted 19 DEC 2020

Neutral Wind Dynamics Preceding the STEVE Occurrence and Their Possible Preconditioning Role in STEVE Formation

Jun Liang[1], Y. Zou[2], Y. Nishimura[3], E. Donovan[1], E. Spanswick[1], and M. Conde[4]

[1]Department of Physics and Astronomy, University of Calgary, Calgary, Alberta, Canada, [2]Department of Space Science, University of Alabama in Huntsville, Huntsville, AL, USA, [3]Department of Electrical and Computer Engineering and Center for Space Sciences, Boston University, Boston, MA, USA, [4]Department of Physics, University of Alaska Fairbanks, Fairbanks, AK, USA

Abstract Strong Thermal Emission Velocity Enhancement (STEVE) is a nightsky optical phenomenon of great research interest in recent years. Recent findings indicated that STEVE likely represents certain extremely intensified chemiluminescence airglow instead of traditional aurora. In this study, we investigate the patterns and variations of the neutral wind and temperature before the STEVE emergence using joint scanning Doppler imager (SDI 630 nm) and optical all-sky imager (ASI) observations, and make an initial effort to explore the potential preconditioning role of neutral winds in the STEVE production. Neutral winds enhance in westward and southward directions following substorm auroral intensification, and show an equatorward propagating trend from auroral latitudes. However, in STEVE events the enhanced equatorward winds feature a steep stop/reversal at certain subauroral latitude, and strong wind convergence is developed there. This pattern sustains for ~15–20 min, and then STEVE arises at about this stop latitude. The strength of the southward wind intensification and wind convergence is in general weaker or absent in nonSTEVE substorm events. We propose that enhanced equatorward winds may transport relevant neutrals species that are key to the STEVE airglow production to subauroral latitudes, and pile up at the stop latitude of the equatorward winds due to the strong convergence there. Such a transport/pileup effect led by the neutral winds may prepare a reservoir of neutral constituent which, when further aided by subauroral ion drift, leads to a dramatic increase of the airglow production and the STEVE occurrence.

1. Introduction

A nightsky optical phenomenon named Strong Thermal Emission Velocity Enhancement (STEVE) has been a topic of great research interest in the past 1–2 years. Its presence was reported in the literature over a century ago (see a historical review by Hunnekuhl and MacDonald [2020]), but escaped the attention of scientists for a long time, until it was brought forth again by citizen scientists and auroral photography enthusiasts in recent years. To date, while its generation mechanism remains unknown, some important advancements have been made toward the understanding of STEVE. (1) STEVE is located equatorward of traditional auroras, and there has been no evidence of appreciable electron/proton precipitation that could be the cause of the luminosity (Gallardo-Lacourt et al., 2018a, 2018b; MacDonald et al., 2018), suggesting that STEVE is not traditional aurora. (2) STEVE is found to be co-located with strong ionospheric electron heating and fast subauroral ion drifts (SAID) in joint optical and in situ satellite observations (Archer et al., 2019a; Chu et al., 2019; MacDonald et al., 2018; Nishimura et al., 2019; 2020a). (3) STEVE occurs during substorm intervals, and typically starts to emerge ~1 h after the substorm onset (Gallardo-Lacourt et al., 2018a). (4) The emission altitude of STEVE is typically at ~210–260 km, though sometimes a separate yet weaker STEVE arc may co-exist at lower altitude (Archer et al., 2019b; Hunnekuhl and MacDonald 2019; Liang et al., 2019). (5) Recently, using spectrograph data it was unveiled that STEVE's main source of brightness comes from an overall enhancement of a continuous visual spectrum, that is, an airglow continuum (AGC, Gillies et al., 2019; Liang et al., 2019), with small or none out-of-background green-line 557.7 nm emissions contained in the STEVE spectrum. While the existence of night AGC has been known for decades (Barbier et al., 1951), their commonly reported intensities in the existing literature (e.g. Sternberg &

Ingham, 1972; Gadsden & Marovich, 1973) are much weaker than that of STEVE (Gillies et al., 2019; Liang et al., 2019)—STEVE is visible even to naked eyes.

It is fair to state that the above existing findings strongly suggest that STEVE likely stems from certain extremely intensified chemiluminescence in the upper thermosphere, instead of traditional aurora. In chemiluminescence, its brightness is proportional to the densities of the air constituents involved in the chain of chemical reactions leading to the chemiluminescence (e.g., Young, 1969). The fact that STEVE occurs at altitudes higher than 200 km excludes the possibility that STEVE be purely neutral airglow without much interaction with plasma, otherwise it would tend to occur in much lower atmosphere where the neutrals are much denser. On the other hand, Since the STEVE arc is found as located in a low electron density "trough" region of the subauroral ionosphere (Archer et al., 2019a; Chu et al., 2019; MacDonald et al., 2018), the out-of-background enhancement of the STEVE chemiluminescence is not likely to be attributed to a strong local plasma density, but is more likely to be related to enhancements of neutrals there, at least for some key constituents relevant to the chemiluminescence. While the underlying mechanism of STEVE remains unclear to date, and it is not the aim of this paper to investigate in detail the specific STEVE mechanism, the above observations and considerations point to a gross perspective that, STEVE likely stems from a drastic plasma-neutral interaction. The ionospheric plasma with reduced density but with high electron temperature and convective flow speed (i.e., SAID), together with enhanced densities of relevant neutral constituents, conspire to make the STEVE occur. Partly owing to the above thoughts, the NO_2 continuum (Gadsden & Marovich, 1973; Hedin et al., 2012; Sternberg & Ingham, 1972) via a radiative recombination reaction $NO + O \rightarrow NO_2 + h\nu$ has been deemed one of the leading candidates of the STEVE AGC to date by some researchers including ourselves. While the NO_2 continuum itself is a neutral process, the NO production in the thermosphere is well known to be sensitive to the magnetosphere-ionosphere-thermosphere interactions in numerous ways (e.g., Barth et al., 2003, 2009; Campbell et al., 2006; Lin et al., 2018; Lu et al., 2010; Solomon et al., 1999; Zhang et al., 2014; Zipf et al., 1970). An enlightening work in this regard was recently done by Harding et al. (2020), who proposed that the nitrogen molecules may be excited to higher vibrational levels via the collision with fast-drifting ions in SAID. These excited N_2 may overcome the activation barrier and react with oxygen atoms to produce NO, and in turn generate the NO_2 continuum that accounts for the STEVE AGC. However, their proposal still summons a substantial enhancement of local neutral density as a prerequisite for the mechanism to produce enough AGC yield to account for the STEVE brightness.

While direct in situ neutral observations at STEVE altitudes are not available at the moment, ground-based measurements of neutral winds and temperature may still offer useful clues to the neutral conditions that potentially contribute to STEVE. This becomes the motivation and the main goal of the current study. To the authors' knowledge this is the first study of the neutral atmosphere in which STEVE develops. We shall first make a key clarification here. As afore-mentioned, based upon existing knowledge there is little doubt that STEVE embodies complex and interactive magnetospheric-ionospheric-thermospheric coupling processes. This study is not intended for an investigation of the thermospheric effects *led by* STEVE. Instead, we shall focus on the neutral wind/temperature patterns and variations *before* the STEVE emergence, based upon a premise that those precedent variations might precondition the thermosphere and lead to a change of relevant neutral constituents, for the ensuing rise of STEVE. It is important to note that such a preconditioning effect, if indeed contributing to STEVE appearance, cannot be instantaneous considering the usually long variation timescale of neutrals in the upper thermosphere (e.g., Nishimura et al., 2020b). Neutral wind variations would presumably occur in advance and persist for a while to let relevant neutrals transport and buildup, so that the corresponding chemiluminescence airglow may gradually grow to detectable brightness, that is, exceeding certain visual/instrumental threshold. In a statistical study, Zou et al. (2020) found that the substorm-associated neutral wind variations often commence right after the onset and reach a quasisteady state within one hour of the onset (see also Cai et al. [2019]). This was also found as compatible with the calculated ion-neutral coupling timescale (Nishimura et al., 2020b). Coincidently, Gallardo-Lacourt et al. (2018b) showed that STEVE typically emerges ~50–80 min after the substorm onset. This time sequence is consistent with our above hunch.

This paper is organized as follows. Section 2 will introduce the instruments used in this study. In Section 3, we shall present two STEVE event examples, with a focus on the characteristic pattern of neutral winds in tens of minutes before the rise of STEVE, and compare with nonSTEVE substorm events. In Section 4 we

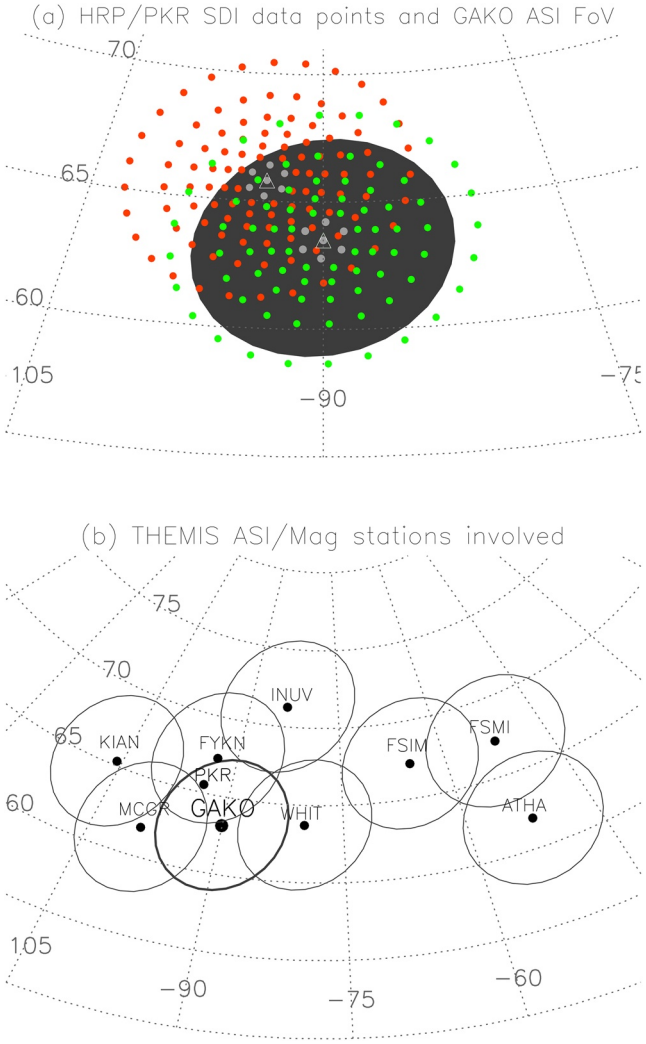

Figure 1. (a) The observation geometry of the FoV of Gakona all-sky imager (ASI), overplotted with the Poker Flat Range (PKR) SDI data points (red) and HRP (green) 630 nm scanning Doppler imager (SDI) data points, in altitude-adjusted corrected geomagnetic (AACGM) coordinate for the year 2010. Two triangles mark the PKR (higher latitude) and HRP (lower latitude) station center. The grayed points denote the zenith and innermost annulus data of each SDI that are ignored in our quantitative analysis of the wind. (b) The THEMIS ASIs and magnetometer stations involved in this study. GAKO ASI is highlighted. The PKR site where the PKR SDI and Poker Flat Incoherent Scatter Radar (PFISR) are located are also labeled. For station name legends, see Donovan et al. (2006). In both (a and b) the map coordinate is AACGM.

shall discuss the potential implication of our results to the possible mechanisms of STEVE. Section 5 concludes the paper.

2. Instruments

The neutral measurements in this study come from the scanning Doppler imager (SDI). A detailed description of the basic principles and operations of SDIs was discussed by Conde and Smith (1995, 1998) and more recently by Anderson et al. (2012a) and Dhadly et al. (2015). In a nutshell, SDI is an all-sky imaging, wavelength-scanning Fabry-Perot spectrometer. It records the spectra of 630 and 557.7 nm optical emissions at over a hundred locations across the sky, from which the line-of-sight (LOS) component of neutral winds and the neutral temperature can be derived from the Doppler shift and Doppler broadening of the emission spectra, respectively. In line with the fact that typical emission altitudes of STEVE are at >200 km, only 630 nm SDI data are used in this study, and we assume a 250 km altitude in mapping the data. The SDIs at Poker Flat Range (PKR, 65.12°N, 147.43°W Geo.) and HAARP (HRP, 62.39°N, 145.15°W Geo.) are included in this study. In particular, the HRP SDI is roughly collocated with the Gakona THEMIS ASI, constituting a desirable conjunction geometry for our research interest. Figure 1a shows the geometry of the field-of-view (FoV) of Gakona ASI, overplotted with the data points of PKR and HRP SDIs, in an altitude-adjusted corrected geomagnetic (AACGM) coordinate (Baker & Wing, 1989). The SDI LOS velocities are inverted to horizontal velocity vector maps via a monostatic fit technique which assumes that vertical winds are constant across the FOV and, for the software version used in this study, that the zonal gradient of meridional winds is negligible (Anderson et al., 2012a; Dhadly et al., 2015). Note that such an assumption is not required when LOS data from two or more stations are involved, as we shall utilize to calculate the wind divergence in Section 3.1. The monostatic fit technique is of course not without uncertainties. Known inaccuracy would occur at near-overhead data points where the viewing geometry is bad for estimating horizontal winds, and near the low-elevation edge where the data points are sparsely distributed and the oblique LOS integral effect may bring uncertainties. That said, on overall the fitting technique is usually found to yield a close approximation to the actual wind field (Anderson et al., 2012a; Dhadly et al., 2015). The SDI monostatic data and summary plot can be found in http://sdi_server.gi.alaska.edu/sdiweb/. In the course of our event selection, we have carefully checked the summary plots and reject events with suspicious wind vector maps. Cloudy nights are discerned visually based on collocated all-sky-camera optical observations as well as keograms of the SDI emission intensity: if the intensity appears overall blurry across latitudes, the emission has probably been scattered by clouds, and the event is dismissed. In particular, a good viewing condition over the Gakona all-sky imager (ASI) is a necessary condition of this study. Also, in this study the zenith and the innermost annulus data points, as well as the data points with elevation angle <20°, are all excluded for any quantitative use. In the STEVE event with both PKR and HRP SDI data, we also apply the bistatic technique (Anderson et al., 2012a) to derive the horizontal winds to aid this study.

The THEMIS whitelight ASI (Donovan et al., 2006) will be used in this study for several purposes. Most importantly, the ASI at Gakona station (GAKO, 62.40°N, 145.16°W Geo.) is used to identify STEVE events or nonSTEVE events. A 250 km emission altitude is assumed for STEVE, which is the same as that applied for the 630 nm SDI data. Liang et al. (2019) reported the possible occurrence of double-layer STEVE

structures in some events, and evaluated that the lower-altitude STEVE likely centers around ~150 km height. However, such a lower-altitude STEVE, even if visibly co-existing, is usually weaker than the higher-altitude STEVE which is typically within ~220–270 km altitude (Liang et al., 2019). Therefore, if only one STEVE arc is seen in the ASI FoV, it is reasonable to assume that it represents the high-altitude STEVE. Note that in a supplementary material (Figure S2f) we perform a triangulation analysis and evaluate the emission altitude of STEVE in the March 26, 2008 event as being around 250 km. In the two STEVE events we are to report, the STEVE arc, at least during its initial emergence in the SDI FoV, are fairly close to the ASI center, so that the error led by the emission latitude uncertainty is presumably small compared to the latitudinal resolution of the SDI measurement. THEMIS ASIs over Alaska and the western Canada sector, together with the co-located THEMIS magnetometer stations, are also involved in this study, mainly serving to infer the substorm context of investigated events, such as the substorm onset time. Figure 1b shows the THEMIS ASIs and magnetometer stations involved in this study. For station name abbreviations, see Donovan et al. (2006). The digital meridian spectrometer at PKR and all-sky cameras at GAKO, both operated by the University of Alaska, Fairbanks are also browsed in some events.

Besides, The Poker Flat Incoherent Scatter Radar (PFISR, 65.1°N, 147.5°W Geo.) data are used in two STEVE events to characterize the plasma flow intensification observed in connection with auroral activity after substorm onset near the equatorward boundary of auroras. PFISR is nearly collocated with PKR SDI. In April 4, 2010 event, PFISR was run in the Aurora & Convection experiment mode, and its long pulse mode data with 1-min integration time are used in this study. In March 26, 2008 event, PFISR was run in the IPY04 experiment mode, and its long pulse mode data with 5-min integration time are used. The plasma convection vector is derived from the long-pulse LOS velocity measurements by assuming that the velocity vectors are homogeneous in the east-west direction across the radar FoV (Heinselman & Nicolls, 2008).

3. Observations

The two STEVE events are from the list in Gallardo-Lacourt et al. (2018b). Readers are referred to their paper for detailed criteria in identifying STEVE from ASI observations. Some of the key characteristics include: the STEVE must be equatorward of, and detached from, the main aurora zone; the STEVE arc is narrow in latitudinal width (~0.1°-0.2°); the arc and/or the fine structures along it show fast westward propagation (a few km/s). In all the following figures with ASI images and/or SDI winds, the AACGM coordinate is used to define the magnetic latitude (MLAT) and longitude (MLON), and to present the data.

3.1. April 4, 2010 Event

This event occurred during a minor geomagnetic storm interval (SYM-H ~ −10 to −20) but the substorm intensity is strong (AL index reaching ~ ~810 nT). From available optical data, the onset started at the Fort Simpson (FSIM, 67.3° MLAT, −65.0° MLON) sector at ~06:18 UT. The top panel of Figure 2 shows the keogram of GAKO THEMIS ASI sampled along its center magnetic meridian (−90° MLON). A default emission altitude of 110 km is assumed here which applies to auroras (Whiter et al., 2013)—but not to STEVE, which we shall use a different emission altitude later. The event occurred in early evening hours. The GAKO THEMIS ASI was turned on at 06:16 UT, yet there was still some apparent twilight contamination in the western portion of the ASI FoV by that time. Nevertheless, the intensification after 06:20 UT and the equatorward expansion of auroras after 06:35 UT can still be seen. The STEVE trace of our interest is labeled, which is at distinctly lower latitudes than auroras. The STEVE is a bit faint in this plot since the color scale here is for substorm auroras; it will become more easily observable in the following plots. The rest of the panels in Figure 2 display a series of images from GAKO THEMIS ASI, showing the STEVE evolution. Note that a 250 km emission altitude is assumed here since we are to focus on STEVE. Starting from ~07:20 UT, a STEVE arc emerges from the eastern portion of the ASI FoV; it then expands westward and enters the FoV of HRP and PKR SDIs (station centers marked by triangles) by ~07:24 UT, with an overall mean westward expansion speed of ~3 km/s. The potential process underlying the fast westward propagation of STEVE will be discussed in Section 4. The STEVE arc then slowly migrates equatorward. Based on the FoVs of available THEMIS ASIs, this STEVE event is relatively short-lived and vanishes at ~07:40 UT. Readers are referred to a supplementary movie to view the full STEVE evolution. In our following presentation, when we refer

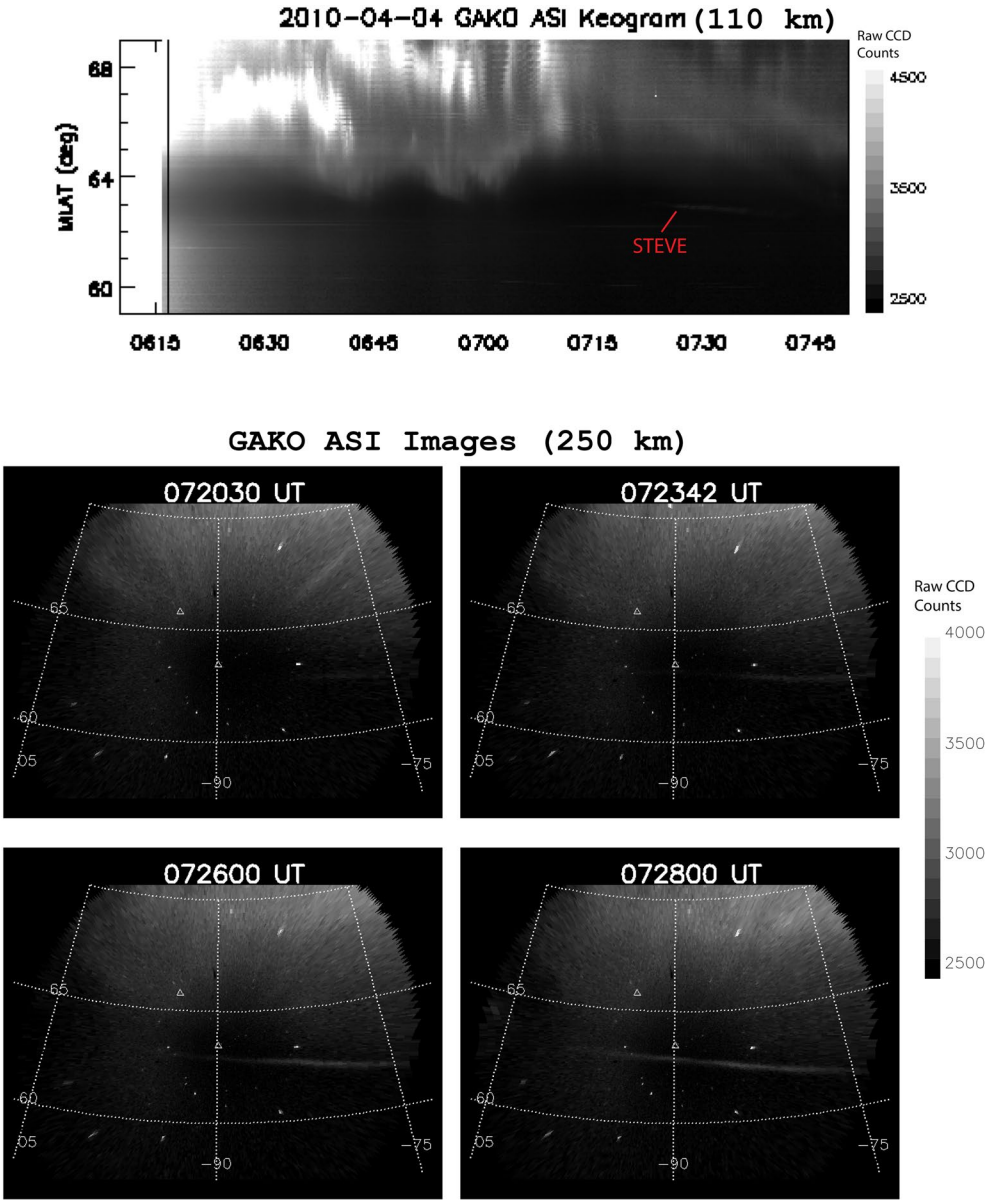

Figure 2. The top panel shows the keogram of GAKO ASI based on 110 km emission height. The rest of panels display a series of GAKO ASI images with emission height of 250 km, showing the evolution and westward propagation of Strong Thermal Emission Velocity Enhancement (STEVE) for April 4, 2010 event. The locations of HRP (lower-latitude one) and PKR (higher-latitude one) SDIs are marked as triangles. Images are shown in AACGM coordinates.

to the "emergence time" of STEVE, we mean the time when STEVE locally arises in the FoV of SDIs, since that is where our available neutral measurements are confined.

In Figure 3, we plot side-by-side the observations from PKR (leftside) and HRP (rightside). Their top panels show the GAKO THEMIS ASI keogram sampled along −93.6° (−90°) MLON, which is the center longitude of PKR (HRP) SDI, assuming a 250 km emission altitude. Since the STEVE is fairly close to the image center in this event, the error led by the emission height uncertainty is trivial. In a supplementary material (Figure S1) we also show the keograms based upon 220 and 270 km emission altitudes, and note that the STEVE displacement led by different assumed emission heights is very small and will not affect our analysis and results, considering the latitudinal resolution of SDI. The second panel of each subfigure, which shows the east-west convection velocity deduced from PFISR observations, is duplicate. The rest of the panels show

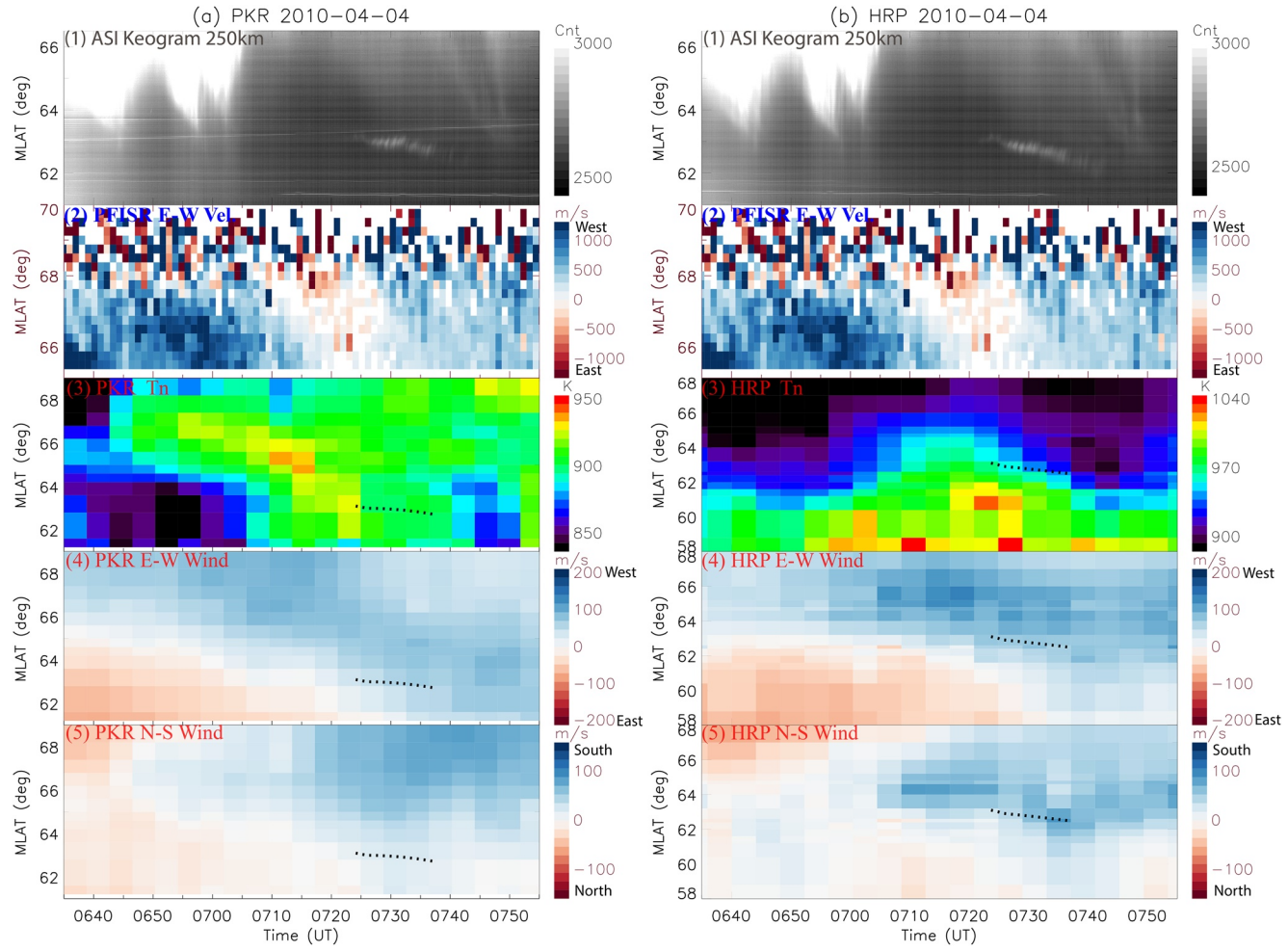

Figure 3. The left-side is for PKR and the right-side is for HRP 630 nm SDI observations. Their figure formats are the same. The panels from top to bottom are indexed to facilitate reference. The top panel shows the ASI keogram sampled along the center meridian of PKR/HRP based on 110 km emission height. The second panel shows the east-west convection velocities (positive westward) from PFISR measurements. The third panel shows the neutral temperature measurements from PKR/HRP SDI. The bottom two panels of each subfigure show the east-west (positive westward) and north-south (positive southward) components of the neutral wind velocity observed by PKR/HRP SDI. From the third to the bottom panel, a black dotted curve marks the trace of the STEVE arc.

the keograms made from the PKR and HRP SDI data. In making these keograms, we adopt the monostatic fit data from the two SDIS and sample the relevant parameters (temperature, velocity) at each latitude bin within ±3° MLON around the PKR (HRP) center meridian. The station latitudes of PKR and HRP SDIs are ~65.8° and 63.5° MLAT, respectively. Note that for all the SDI keograms we have also overplotted the STEVE trace obtained from the ASI keogram sampled at the same PKR/HRP meridian (top panel) to facilitate a comparison with the STEVE emergence time and latitude. We have also checked the PFISR flow and HRP SDI wind data at earlier times (not shown) to obtain a broader context of the convection and wind evolution. There was an earlier and smaller substorm onset at ~04:55 UT inferred from available optical and magnetometer data, and westward plasma flows of several hundred m/s had been seen on PFISR since ~05:00 UT. However, noticeable westward and southward wind enhancements occur only after the much stronger substorm with onset at ~06:18 UT. We of course do not deny that, due to the relatively long response timescale of neutral winds to ion drag, the preexisting westward plasma flows might also partly contribute to the later wind development. Following this substorm intensification and expansion, strongly enhanced westward flows (>1 km/s) appear at ~65°.5-67° MLAT. Note that ~65.5° MLAT is the equatorward edge of the PFISR FoV, so that there is unfortunately no plasma flow measurement at lower latitudes.

The third panel of Figure 3 shows the neutral temperature (T_n) measurements from PKR and HRP SDIs. Note that T_n is plotted in different color scales for two SDIs. We shall first remind that the interpretation of

the T_n variations seen on SDI measurements is often complicated by the uncertainty of emission heights. Inferred from the NRLMSISE-00 empirical model, T_n may increase by 40–50 K over 200–250 km altitude range where the 630 nm auroras/airglows may peak. The PKR SDI indicates an equatorward propagation of T_n enhancement that originates from ~67° MLAT. Since such an enhancement is apparently associated with the PFISR westward flow intensification, and that an equatorward propagation of westward wind enhancement is jointly seen (to be detailed subsequently), we conceive such a T_n enhancement and its equatorward-propagating trend to be real, instead of being an alias of varying 630 nm emission heights. On the other hand, T_n enhancements at latitudes lower than 63° MLAT are seen on HRP SDI observations. The increment magnitude of such enhancements is between ~60–90 K, so that they are unlikely to be fully attributed to the variations of 630 nm emission heights. One may notice the significantly different pattern of T_n seen on two SDIs. This is of course partly owing to the different latitudinal coverage and longitudinal sampling region (in making the keogram) of the two SDIs. However, a close examination of the data indicates that, even in their common area of observations, T_n seen by the two SDIs still show different patterns and absolute values. We point out that such a discrepancy is not entirely unexpected. Anderson et al. (2012a) compared the T_n measurements from PKR and HRP SDIs in their common volumes of observations, and noticed a correlation as low as 0.53 and absolute difference as large as ~100 K (see their Figure 6). Part of the T_n discrepancies may be attributed to the intrinsic uncertainty of SDI temperature measurements (up to ~4%). Another likely reason for the discrepancy is that the latitudinal-altitudinal distribution of T_n intensifications may cause different integral effects at different viewing aspects. The lower-latitude T_n intensification shown on HRP SDI is not well seen on PKR in this event, likely because that structure is near the lower-elevation edge of the PKR SDI where a latitudinal smearing effect along the LOS direction is expected. For the higher-latitude T_n intensification structure seen on PKR SDI, we speculate that the altitude ranges of the T_n enhancement there (presumably led by Joule heating) might be below the peak height of the auroral 630 nm emissions. In an oblique view from the HRP SDI, the contribution from this Joule heating region is overridden by the contributions from the main auroral 630 nm emission region at higher latitudes and altitudes, so that the former is not well seen on HRP 630 nm SDI. We footnote that an apparently equatorward propagating T_n intensification structure originating from higher latitudes is indeed seen on the 557.7 nm HRP SDI data (not shown) which observe much lower altitudes. Partly due to the potential uncertainty of T_n measurements, this study is restricted to qualitative descriptions of certain T_n features in STEVE events, and we shall put more quantitative analyses on the neutral winds.

The bottom two panels of Figure 3 show the east-west and north-south components of the neutral wind velocity, respectively. Note that in the data processing we have excluded data points at the zenith and the innermost annulus—by doing so we only keep data points at >25° zenith angle—since the near-overhead data points are not geometrically suitable for the horizontal wind fitting and thus may contain relatively large errors. The PKR and HRP SDIs display generally compatible patterns of wind variations, yet certain discernible differences exist. Some of the discrepancies between the two SDI measurements may be attributed to the LOS integral effect under an oblique viewing geometry. For example, the winds seen on HRP SDI near its northern edge of FoV (66°-68° MLAT) are weaker than those seen on PKR SDI. Besides, the potential existence of longitudinal inhomogeneity (PKR and HRP are separated by ~3.6° MLON) and the error of the monostatic fit wind data may also contribute to the differences between the two SDI winds. Note that the above two error sources are intertwined since the zonal homogeneity of meridional winds is one of the underlying assumptions of the monostatic fit. Nevertheless, both SDIs show that westward winds at auroral latitudes start to intensify shortly after the westward plasma flow intensification seen on PFISR, and such westward wind intensification gradually propagate equatorward. Equatorward winds also intensify but appear to slightly lag the westward wind intensification. The key observation of our interest is that, the equatorward wind intensification seems not to penetrate to lower latitudes (≤62° MLAT) before 07:25 UT. In particular, the HRP observation clearly shows a peak of the southward wind at ~64° MLAT, and an abrupt reduction of the southward winds at ~63° MLAT starting from ~07:05 UT, ~15–20 min before the emergence of STEVE. The isolated peak of southward winds is not seen on PKR, yet a diminishing southward wind toward low latitudes can still be perceived. For simplicity, we shall refer to the latitude corresponding to a sharp wind deceleration as a "stop latitude" in our presentation, yet we of course do not mean a complete termination of winds. Such a "stop latitude" of the equatorward winds later becomes the

initiating latitude around which the STEVE starts to rise. After ~07:30 UT the equatorward winds appear to penetrate through to further lower latitudes, and the stop latitude also migrates equatorward accordingly.

To better demonstrate the neutral wind pattern preceding the STEVE appearance and surrounding the STEVE latitude, we present in Figures 4 and 5 a series of THEMIS ASI images superposed by the horizontal neutral wind vectors from PKR (red) and HRP (green) SDIs. We shall call readers' special attention to the winds surrounding and within the yellow box region overplotted on the images. This box region serves two purposes. First, it is the region inside which we are to evaluate the wind divergence subsequently. More importantly, this region contains the lately emerging STEVE (see Figures 5c–5d), so that one may readily check the wind pattern around the STEVE latitude before the actual emergence of STEVE, in the context of the presumed preconditioning role of the winds. The substorm onset starts at ~06:18 UT as inferred from the ASI observations; some small changes of the wind occurred after ~06:20 UT (not shown), but until 06:37 UT (Figure 4a) neutral winds remains moderate or mild. They are moderate and mostly directed north-westward at the auroral latitudes, while mainly eastward at subauroral latitudes in the lower-latitude portion of the FoV. Westward winds start to enhance and prevail after ~06:50 UT (Figure 4b), but the winds at subauroral latitudes remain weak. Our main research interest is on the wind dynamics after ~07:05 UT. In a series of successive images after 07:05 UT, winds become intensified in westward and southward directions, and such intensification gradually expands from higher to lower latitudes. However, the wind magnitude decreases steeply across the box region. There is a dramatic difference between the winds at latitudes above and below the box, or equivalently across the later STEVE arc latitude. Even by visual inspection, one may readily sense that a negative divergence of winds, or equivalently wind convergence, develops in the box region ~15–20 min before the emergence of STEVE in this region.

The above-presented SDI winds are from the monostatic fit data set. We have also tried the PKR/HRP bistatic approach following the procedures proposed in Anderson et al. (2012a). We remind that LOS velocities from two stations are inadequate to solve the three components of winds, so that certain assumptions and geometry limitations are still necessary. More specifically, the derivation of horizon winds from a bistatic method requires a common observation volume of two radars, and that the observation plane containing the two LOS directions from each station toward the common-volume data point must deviate substantially from the local vertical direction. This is particularly necessary for our event, since the horizontal winds in the overlapped area of two SDIs are mostly south-westward directed, roughly perpendicular to the PKR-HRP line, so that any LOS measurement too close to the PKR-HRP great circle plane would have a significant yet undetermined contribution from the vertical wind. In the following demonstration, we adopt the same procedures and geometric criteria to derive the bistatic horizontal winds as those in Anderson et al. (2012a). Readers are referred to their paper to see the technical details. Figure 6 displays four frames (corresponding to Figures 4b, 5a, 5c, and 5d, respectively) of the bistatic winds superimposing on GAKO ASI images. Due to the geometry limitation, most of the available bistatic data points are relatively far away from the STEVE arc, so that they are not particularly suitable for our research goal of examining the neutral wind dynamics surrounding the emerging STEVE arc. That said, the bistatic winds may serve as a reality check of the monostatic fit data. As one can see, the overall pattern and magnitude of the bistatic winds are fairly similar to that shown in the monostatic data: (1) winds are intensified during the substorm, and the intensification propagates equatorward; (2) winds are strong and mostly south-westward at higher latitudes, yet diminishing toward lower latitudes. We thus claim that the bistatic horizontal winds are generally consistent with the monostatic data, though upon a close look the bistatic data appear to unveil zonal inhomogeneity of meridional winds around ~65° MLAT, which contradicts the underlying assumption, and constitutes one likely error source, of the monostatic fit.

In the following we shall make quantitative efforts to evaluate the neutral wind divergence surrounding the STEVE latitude. This is motivated by the notion that the wind divergence alludes to a change of the neutral density, as per the continuity equation $dn / dt \sim -n \nabla \cdot \boldsymbol{u}$ (to be further discussed in Section 4). Due to the potential error in the monostatic data, and the inadequacy of bistatic data points in the vicinity of STEVE, the two data sets are deemed nonideal for our purpose. Instead, we shall directly use the raw LOS velocity measurements of HRP and PKR SDIs. The algorithm is conceptually similar to that introduced in Conde and Smith (1998), but no additional assumption on the wind derivatives is required. For the horizontal components of the neutral wind, we use a Taylor expansion approximation to the first-order,

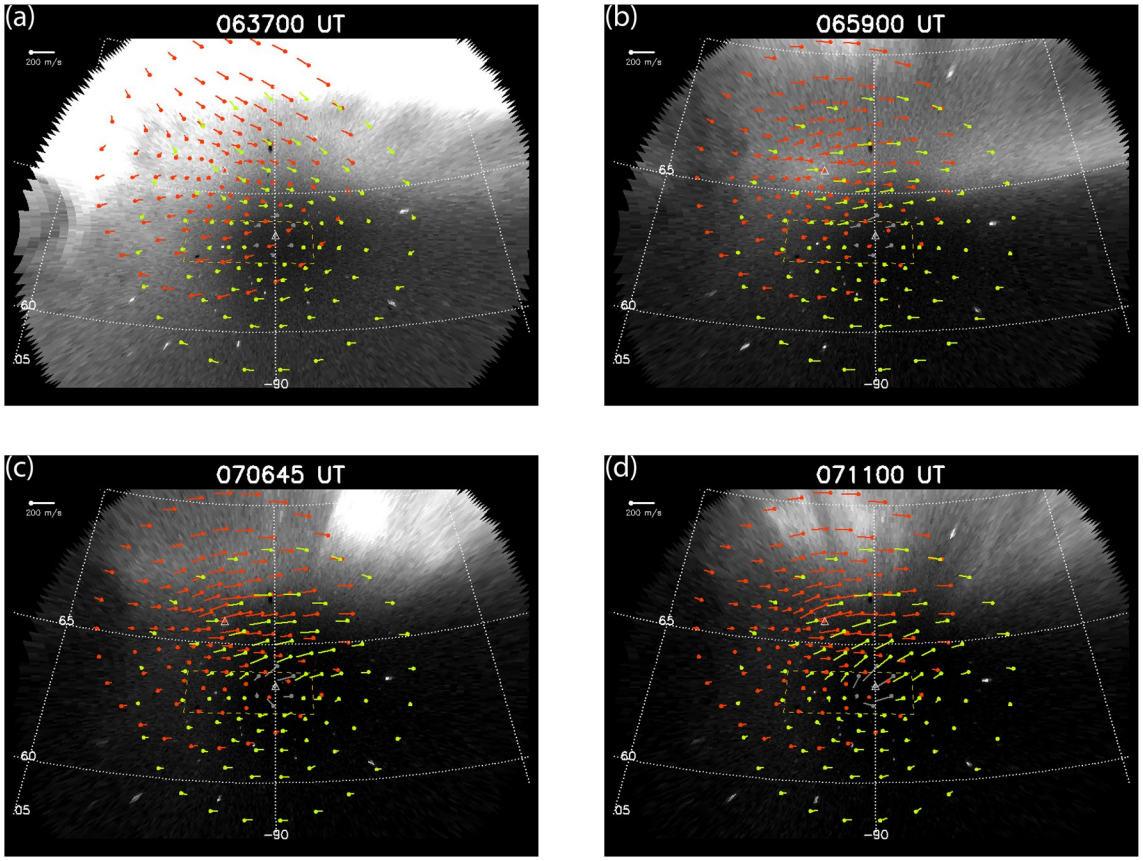

Figure 4. A series of ASI images superposed by the monostatic horizontal neutral wind vectors from PKR (red) and HRP (green) 630 nm SDIs. An emission height of 250 km is assumed for both ASI and SDI. A yellow dashed box marks our sampling region for wind divergence calculation (see text for details).

$$u_x = u_{x\_0} + \frac{\partial u_x}{\partial x}\cdot\left(x - x_0\right) + \frac{\partial u_x}{\partial y}\cdot\left(y - y_0\right) \tag{1}$$

$$u_y = u_{y\_0} + \frac{\partial u_y}{\partial x}\cdot\left(x - x_0\right) + \frac{\partial u_y}{\partial y}\cdot\left(y - y_0\right) \tag{2}$$

in which x (positive north) and y (positive west) denote the meridional and zonal directions, respectively. A local plane approximation is adopted. x_0 and y_0 give the center of the region of interest, and u_{x_0} and u_{y_0} denote the x and y components of the wind at this center point. The sampling region (i.e., the yellow box in Figures 4 and 5) covers a latitude range of 62.5–64° MLAT that contains the initial rise of STEVE, and a longitude range spanning from 2.5° west of PKR center meridian to 2.5° east of HRP center meridian. The SDI measures the LOS velocity component of the vector wind, that is,

$$u_{\mathrm{LOS}} = u_x \cdot l_x + u_y \cdot l_y + u_z \cdot l_z, \tag{3}$$

in which l_x, l_y, and l_z denote the unit vector of the LOS direction in local x-y-z coordinate (z-direction is vertically upward). We assume $u_z, u_{x\_0}, u_{y\_0}, \partial u_x / \partial x, \partial u_x / \partial y, \partial u_y / \partial x, \partial u_y / \partial y$ are constant in the box region of interest. Using an array of LOS measurements contained in the region, we solve the above parameters via a least squares fitting method.

There is however, one issue in the practical implementation of the above technique, related to the uncertainty of u_z and its possible horizontal inhomogeneity. This is because the region of our special interest contains the overhead data points and includes reducing horizontal winds. u_z is typically much smaller than horizontal winds. In a routine monostatic fit (e.g., Conde & Smith, 1998), the LOS wind at the zenith

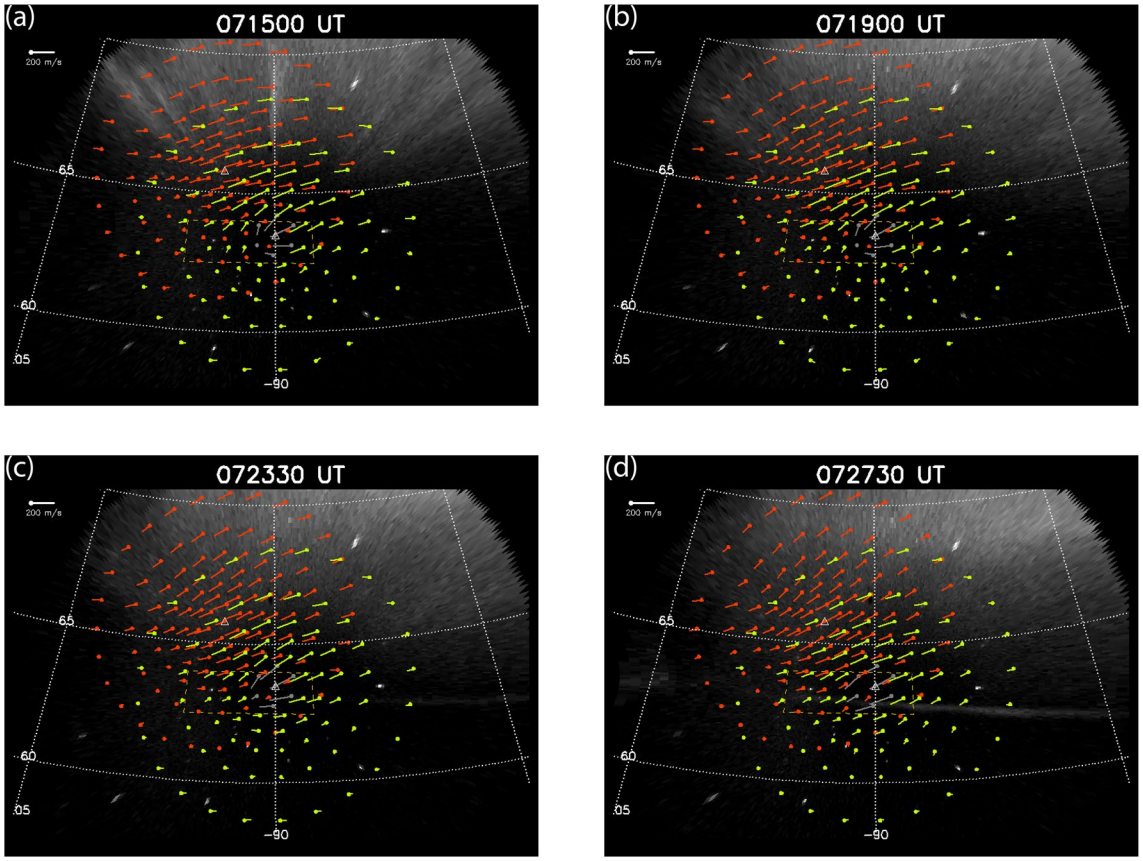

Figure 5. A continuation of Figure 3.

data point is often deemed as the u_z, which is further assumed to be constant for the entire fitting region. In our event, u_z given by the zenith data point of HRP remains small (<∼20 m/s, not shown) and exhibits some gravity wave-like oscillations all the time. However, if the LOS direction is too close to the zenith, even a small u_z may impose a nontrivial effect on the fitting of horizontal winds. This is the reason why the near-overhead points in the monostatic fitted wind vector data may contain large errors. As a numerical test we have tried a few different methods to treat u_z: (1) assuming u_z constant and using direct least squares fitting through Equations 1 2 3 to obtain u_z; (2) using zenith-observed u_z in 3 and fitting other parameters; (3) excluding zenith data point and assuming $u_z = 0$. All three methods yield noticeably different fitting outcomes of the horizontal gradients if we include all data points with uniform weight. To deal with such a difficulty, we first exclude the HRP zenith and innermost annulus data, and only keep data points with zenith angle >26° (tan26°∼ 0.5 so that the horizontal wind projection on the LOS direction prevails as long as it is more than twice the vertical wind). We then adopt a weighted least squares fitting technique: LOS data points are assigned with different weights, in practice defined by $\tan(\theta)$, in which θ is the angle between the LOS and the local vertical direction, so that the data points with LOS direction closer to the local zenith have a relatively smaller contribution to the overall fitting. The above procedure applies only to HRP SDI; for the PKR SDI the box region is well off-zenith, and we shall use a uniform weight (taken as the averaged weight of all HRP data points in use) for PKR data points. Via numerical tests we have found that the above weighted least squares fitting technique may yield relatively stable horizontal gradients against different u_z assumptions, but the downside is that, admittedly we are not able to reliably derive u_z with our procedure.

The top panel of Figure 7 shows the measurement uncertainty of the LOS velocity from the Doppler-shifted 630 nm emission spectrum for all data points included in our calculation. As one can see, the measurement uncertainty is always very small in this event. The second panel of Figure 7 shows the residual standard error of the fitting, which is persistently <∼5 m/s. The above two errors are small compared to the wind velocity, so that the fitting quality can be expected to be reasonably good. Based upon the fitted solution of partial

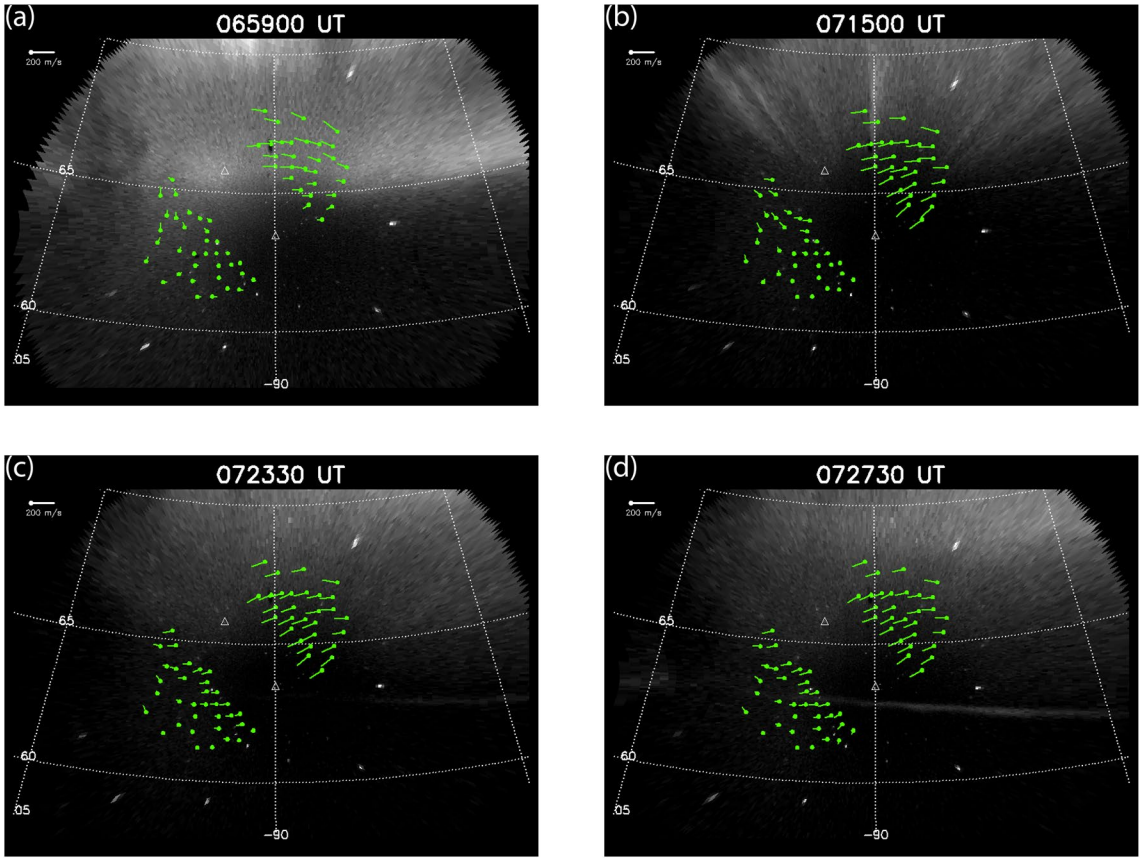

Figure 6. A series of ASI images superposed by the bistatic horizontal neutral wind vectors. An emission height of 250 km is assumed.

derivatives, we show the divergence ($\nabla\cdot\boldsymbol{u}$) and vorticity ($\nabla\times\boldsymbol{u}$)$_z$ of the winds in the bottom two panels of Figure 7, respectively. The divergence reaches a negative valley of $\sim -4\times10^{-4}$ s^{-1} during ~07:10–07:25 UT, preceding the rise of STEVE. This is consistent with our inference from the stop latitude of winds. To further corroborate our result, we have also tested with other methods to evaluate the divergence: (1) Using the monostatic wind vector data of HRP and PKR SDIs (with zenith and innermost annulus data of HRP excluded); we shall elaborate the involved algorithm in the next subsection. (2) Excluding data at the two innermost annuli and keeping only data points at >36° zenith angle—by doing so we further suppress the u_z effect but at a cost of reduced data points in the fitting. As one can see, all approaches yield fairly compatible results. Most importantly, a strong divergence of $\sim -4\times10^{-4}$ s^{-1} before the STEVE emergence is reproduced in all three approaches. We thus believe that the derived divergence is trustworthy. The above-depicted technique of weighted least squares fit with the HRP zenith and the innermost annulus data excluded is deemed successful, and shall be adopted later in the calculation of wind divergence in nonSTEVE events. The obtained wind convergence in this STEVE event is much stronger than the typical values seen at subauroral latitudes in the evening sector (e.g., Dhadly et al., 2017, 2018; Kwak & Richmond, 2014; Thayer & Killeen, 1991). Two footnotes are given here. First, our procedure assumes a uniform divergence over the entire box region whose latitudinal width (1.5°) is much wider than the STEVE arc. This is of course mainly limited by the latitudinal resolution of SDI measurements. Second, the convergence in the box region appears to relax after ~07:25 UT, but this is mostly because that the stop latitude of the winds has gradually shifted equatorward (and so does STEVE) and moved beyond our calculation region.

The wind vorticity also shows variations before the emergence of STEVE. The enhanced vorticity during ~07:00–07:10 UT is related to the equatorward progression of the westward wind and its shear with the preexisting eastward wind at lower latitudes, the latter of which is possibly associated with the day-night temperature gradient in the dusk sector. The vorticity in the box region is reduced as the westward winds expand further equatorward after ~07:15 UT. While the wind vorticity may be of interest for some other

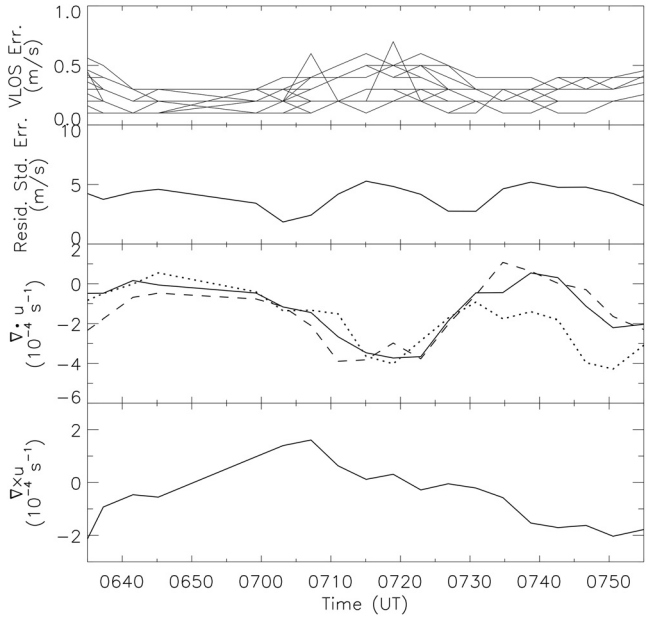

Figure 7. The top panel shows the residual standard error of the least squares-fitting in our calculation of the wind divergence. The middle and the bottom panel shows the calculated divergence and the z-component of vorticity of horizontal neutral winds. For the wind divergence of our key interest, we have compared with the results from two other approaches: the dashed curve denote the approach using the monostatic wind vector data of HRP and PKR 630 nm SDIs, while the dotted curve denote the approach that excludes data at the two innermost annuli and keeping only data points at >36° zenith angle. See text for details.

research purposes, in this study, during our event selection procedure we have noticed that a counterclockwise vorticial wind pattern is fairly common in SDI data at subauroral latitudes and in the local time range of interest, and a vorticity of $\sim 2 \times 10^{-4}$ s^{-1} is often reached or even exceeded in nonSTEVE substorm events (not shown). As a matter of fact, this level is basically about the same magnitude as those mean values obtained from large statistical studies at subauroral latitudes in the evening sector (Dhadly et al., 2017, 2018; Thayer & Killeen, 1991). Therefore, so far we do not deem the wind vorticity a STEVE-specific feature, and will not pay much attention to it in our following presentation.

3.2. March 26, 2008 Event

We shall then report another STEVE event that is solely seen on PKR SDI (The HRP SDI had not launched by that time). This event occurred during a nonstorm interval (SYM-H >10) but the substorm intensity was strong (AL reaching ~800 nT). This event is also studied for other research purposes by Nishimura et al. (2020a, 2020c). Based upon available optical data, the onset of strong aurora intensification was first seen in the FSIM sector at 06:33 UT, which rapidly expanded westward into the Alaska sector in a few minutes. The top panel of Figure 8 shows the keogram of GAKO THEMIS ASI sampled along the GAKO center meridian assuming a 110 km emission altitude. The STEVE of interest is marked. Though not of the main research objective of this study we bring forth one note here. Before ~07:00 UT there were some seemingly detached arcs that reached low latitudes, making one wonder whether they represent STEVE as well, and what is the difference between them and the later STEVE of our interest. These previous low-latitude arcs are analyzed by Nishimura et al. (2020a), who found them to be related to strong energetic proton precipitations as seen in the POES satellite data. STEVE on the other hand, is known not to be associated with energetic proton precipitation or equivalently proton auroras (Gallardo-Lacourt et al., 2018a; Liang et al., 2019; MacDonald et al., 2018). A movie is provided to show the evolution of those previous low-latitude arcs, and some brief descriptions are given in supplementary material. Via triangulation procedures from multiple ASIs (see supplementary material) we evaluate the emission altitudes of those previous low-latitude arcs as well as the later STEVE: the former arcs are found to be centered at an emission altitude of ~100–110 km, while the STEVE is found at ~250 km altitude. We conclude that those previous low-latitude arcs represent different phenomena from the later STEVE.

The rest of the panels in Figure 8 display a series of images from GAKO THEMIS ASI (assuming 250 km emission altitude), showing the STEVE evolution. At around ~07:22 UT. the STEVE arc begins to emerge in the eastern portion of the ASI FoV. It expands progressively westward in the next a few minutes, and reaches the FoV of PKR SDI by ~07:25 UT. Later on, the STEVE becomes more brightened and dynamic, with some signs of co-existing double-layer STEVE and/or "picket-fence" structures (Liang et al., 2019), but a detailed analysis of the STEVE structures is beyond the interest of this study. A supplementary movie displays the evolution of the STEVE. This STEVE and its later picket-fence structure were captured by photographs from a citizen scientist, Mr. Challak, at Palmer, Alaska (see Figure S3). Nishimura et al. (2020a) found that, DMSP F16 satellite data, though in the southern hemisphere, crossed a strong SAID channel that was roughly conjugate to the northern STEVE arc in this event.

The top panel of Figure 9 shows the keogram sampled along the center meridian of PKR SDI, from GAKO THEMIS ASI data. The second panel shows the east-west convection velocity deduced from PFISR observations. Enhanced westward plasma flows of order of ~1 km/s are seen near the equatorward edge of its FoV. The third panel shows the neutral temperature keogram derived from PKR SDI. There is a T_n enhancement that originates from auroral latitudes at ~66° MLAT after ~06:45 UT, and there is another T_n enhancement

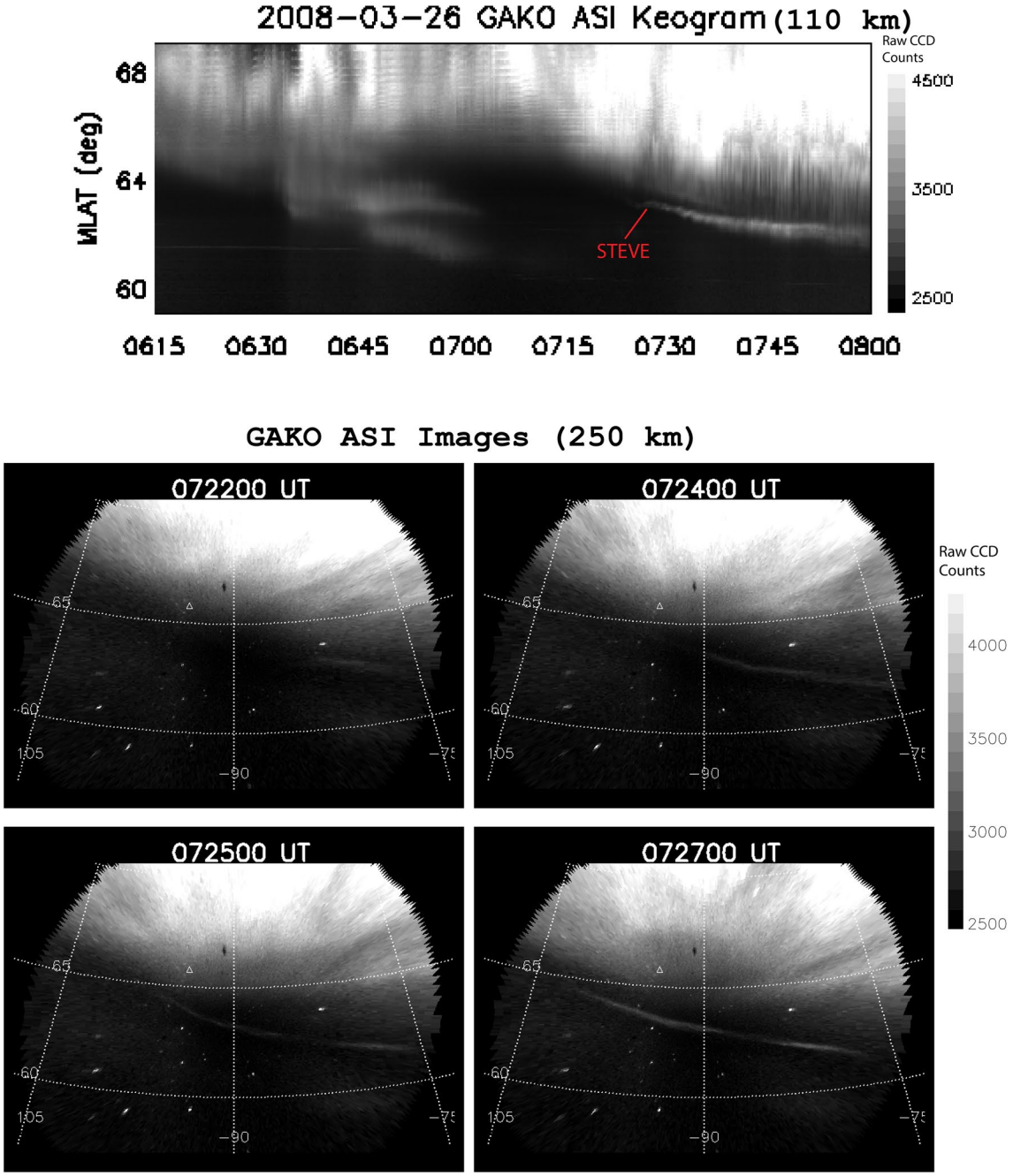

Figure 8. The top panel shows the keogram of GAKO ASI based on 110 km emission height. The rest of panels display a series of GAKO ASI images based on 250 km emission height, showing the evolution and westward propagation of STEVE for the March 26, 2008 event. The location of PRK SDI is marked as triangle.

at latitudes <63° MLAT, which appears to stem from the low-latitude edge of the SDI FoV after ~06:50 UT. The T_n observation is thus consistent with that in the previous event, except that the enhancements at both higher and lower latitudes are seen in one SDI instead of being seen via two separate SDIs as in the previous event. In this event, the T_n intensification at lower latitudes is strong enough to survive the LOS integral effect at low-elevation measurements. The fourth and fifth panels of Figure 9 show the east-west and north-south components of the neutral winds. Westward winds start to enhance after ~06:45 UT, initially at ~66°-68° MLAT, and then gradually propagate toward lower latitudes. The southward winds also intensify, but

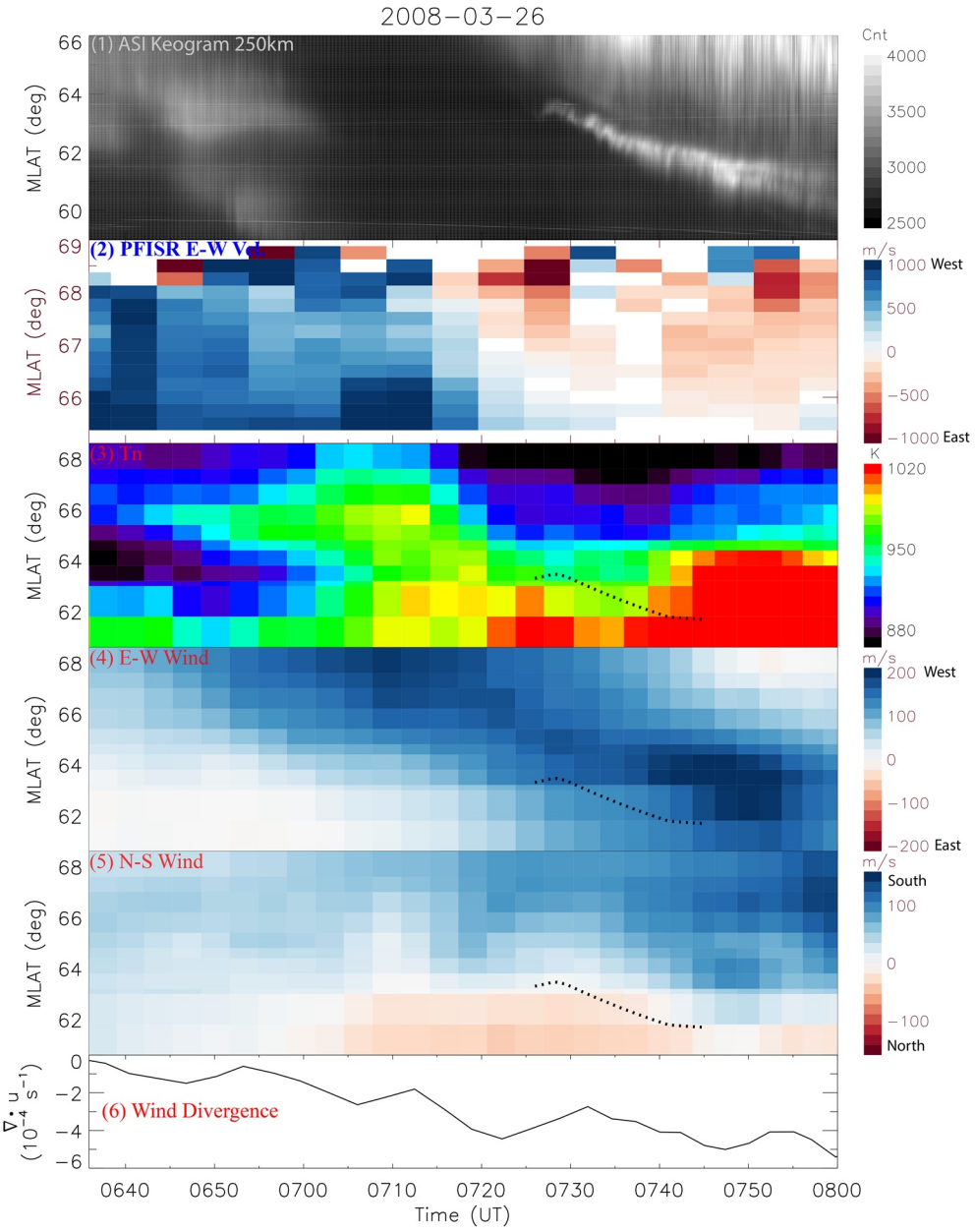

Figure 9. The top panel shows the ASI keogram sampled along the center meridian of PKR. The second panel shows the east-west convection velocities (positive west) from PFISR measurements. The third panel shows the neutral temperature measurements from PKR 630 nm SDI. The fourth and fifth panels of each subfigure show the east-west and north-south components of the neutral wind velocity observed by PKR SDI. From the third to fifth panel, a black dotted curve marks the trace of the STEVE arc. The bottom panel shows the calculated wind divergence at 62.5°-64° MLAT.

we again notice that the southward neutral wind seems not to penetrate to lower latitudes; there is a distinct reversal from southward winds to northward winds across ~63° MLAT. Such a wind reversal latitude is evident after ~07:12 UT. The STEVE later initiates at roughly the same latitude as this reversal latitude of meridional winds.

We also evaluate the wind divergence around the STEVE latitude. We shall first clarify that it is not mathematically possible to fit the wind gradients using single-station LOS measurements with a procedure similar to that in the previous subsection, without additional assumption on the wind derivatives (for mathematical

details in this regard, see Conde and Smith [1998]). Instead, we shall directly use the monostatic-fitted horizontal wind vectors to evaluate the divergence. We sample the vector wind data within 62.5°-64° MLAT and ±3° MLON around the PKR center meridian. The data points in the sampling region are ∼42°-52° off the PKR zenith so that the u_z uncertainty is trivial there. We apply a first-order Taylor expansion of the vector winds, also defined by Equations 1 and 2, in the region of interest, and evaluate wind derivatives using a least squares linear regression. The outcome of the computed divergence is plotted in the bottom panel of Figure 9. The wind convergence starts to enhance after ∼07:12 UT, reaching $\sim 4.5 \times 10^{-4}$ s^{-1} before the emergence of STEVE. The above observations are largely consistent with that in the previous event.

3.3. Summary of Two STEVE Events

In the above we have described the neutral wind and temperature variations in two STEVE events. To summarize the key observations, neutral winds enhance in westward and southward directions following substorm auroral intensification, and show southward propagating trend originating from auroral latitudes. However, the equatorward winds appear to feature a steep stop/reversal at certain latitude, and strong negative divergence of wind develops there. This pattern sustains for ∼15–20 min, and then STEVE arises at about this stop/reversal latitude. Neutral temperature enhancements take place in two latitude ranges: one originating from auroral latitudes, and the other stems from latitudes lower than STEVE.

There are several existing studies on neutral wind variations at high latitudes during substorm intervals, some of which showed conflicting findings (e.g. Cai et al., 2019; Ritter et al., 2010; Xu et al., 2019; Zou et al., 2018, 2020). Ritter et al. (2010) and Xu et al. (2019) both reported fairly small wind variations (no more than a few tens m/s) after substorm onset, and the deviation tends to be eastward in the premidnight sector, yet Cai et al. (2019) and Zou et al. (2020) both noticed the presence of much larger (>100 m/s) variation magnitudes with westward/southward wind intensification. One of the possible reasons for the above discrepancy might be the difference in the observation latitudes relative to substorm-intensified auroras. In the premidnight sector, plasma convection typically follows a Harang system, eastward at higher latitudes and westward at lower latitudes. In particular, flows near the equatorward boundary of auroras often strongly enhance with the auroral intensification and become part of the SAPS (Lyons et al., 2015; Nishimura et al., 2008; Zou et al., 2009; 2012; Gallardo-Lacourt et al., 2017; Zou et al., 2018), as partly corroborated by PFISR data in our events. Westward neutral winds in the F-region ionosphere intensify accordingly due to the ion drag, and the neutral temperature enhances due to a combination of the auroral heating and the Joule heating associated with the strong convection electric field. This may generate an equatorward pressure gradient force toward subauroral latitudes which leads to the southward wind. It is important to note that the meridional and zonal winds are inherently coupled via the Coriolis force. Thus, the southward pressure gradient force may also partially contribute to the westward rotation of winds due to the Coriolis effect. However, in a statistical study Zou et al. (2020) found that a southward wind intensification is more often seen in the midnight-postmidnight sectors, but not common in the evening-premidnight sector. To the authors' knowledge, none of the existing observations of substorm-associated neutral winds specifically addressed the wind divergence at subauroral latitudes. It is mandatory for us to investigate whether or not the subauroral neutral wind pattern we observed during STEVE events is common to all substorm events, which is the goal of the next subsection.

In both STEVE events, neutral temperature enhancements take place in two latitude ranges: one originates from auroral latitudes, and the other is at latitudes lower than the STEVE and appears to stem from the low-latitude edge of the SDI FoV. This may not be a coincidence. As stated above, the equatorward wind is mainly driven by the pressure gradient force that is associated with the Joule heating in the auroral and SAPS flow regions. If in the meantime there is also a strong temperature enhancement at mid-latitudes and in turn an equatorward temperature gradient, the corresponding pressure gradient force (assuming the density gradient is comparatively minor) would act to impede the equatorward winds, thus explaining their deceleration/stop at certain latitude. The equatorward pressure gradient may even lead to poleward winds at lower latitudes, as hinted in March 26, 2008 event (see Figure 9). The origin of such a T_n intensification probably owes its source in the mid-latitude region, beyond the SDI FoV. While this is an interesting research topic by itself, we realize that mid-latitude T_n enhancements may own their source to various

mechanisms, some of which may not be related to substorm processes at all. As we indeed infer from our survey, mid-latitude T_n enhancements at times exist in nonSTEVE events as well. Due to the lack of relevant observations at mid-latitudes in this study, it is difficult to clarify the source mechanisms of those T_n enhancements and make a meaningful comparison between STEVE and nonSTEVE events. This is further confounded by the fact that the temperature measurements usually contain larger uncertainties than the wind velocity measurements (e.g., Andersen et al., 2012a), particularly at lower elevation angles where a LOS integral effect may be detrimental. Due to the above reasons, in the following we shall focus on the neutral winds in our analyses of nonSTEVE events.

3.4. Comparison with NonSTEVE Substorm Events

For a comparison purpose, we survey over the year 2010–2012 to collect nonSTEVE substorm events, and investigate their general pattern of neutral winds at subauroral latitudes. Our event selection criteria are as follows.

1. The neutral wind patterns, both the background one and the substorm-associated variations, have a strong local time dependence (e.g., Emmert et al., 2006; Dhadly et al., 2017, 2018). In particular, Zou et al. (2020) indicated a systematic difference between the neutral wind pattern in the evening sector and that in the midnight sector during substorm intervals. For both STEVE events we presented above, the substorm onset occurs during 06:00–07:00 UT, while STEVE mainly exists during ~07:25–08:00 UT or ~20.5–21.1 h MLT. To screen the influence of the local-time dependence of neutral winds on our comparison effort, we shall only look for events with substorm onset at 6–8 UT, and accordingly mainly investigate neutral wind variations during ~07:00–09:00 UT. Neutral wind variations at other time sectors and comparison for STEVE and nonSTEVE events will be left for future studies
2. The minimum AL index must be less than −200 nT for the substorm to be considered. To define a substorm onset, we use magnetometer and optical data in Alaska and western Canada sectors. While it is often the case that not all ASIs have favorable viewing conditions, clues of auroral intensification and expansion must be seen in at least one optical ASI in Alaska, so that we can reasonably conceive that the substorm activity has indeed approached the time sector of SDI measurements. If the optical viewing condition is ideal so that the initial onset time and location can be unambiguously identified from ASIs, we shall use this optical onset time. Otherwise, if optical observations in the initial onset sector are unavailable, we shall resort to the SuperMAG database for the onset time (Gjerloev, 2012). This magnetometer-based onset time may lag the actual onset time by several minutes, but such uncertainty is trivial to this study, since the onset time is used in this study only to delimit an overall time interval for us to look into the SDI data
3. The viewing condition of GAKO THEMIS ASI (or equivalently the digital all-sky-camera at GAKO run by the University of Alaska) during the event interval must be good enough for us to exclude the existence of STEVE. While it is possible to derive the STEVE-related neutral dynamics with PKR SDI alone, as we have exemplified in Section 3.2, a combination of HRP and PKR data is preferable. Thus, in the survey of this study we preferentially select events with SDI data available at both HRP and PKR, though later in this subsection we shall also enroll and analyze some PKR-only events from Zou et al. (2020)'s database to complement this study. Since GAKO is collocated with the HRP SDI, the criterion that the former has a good viewing condition naturally means that the latter has as well, but we make additional checks (via the intensity map) on the PKR 630 nm SDI data to make sure the sky is not cloudy, at least at southward looking directions, that is, toward subauroral latitudes of interest
4. Our research interest is on the STEVE and neutral wind dynamics at subauroral latitudes, and we resort to GAKO ASI and HRP SDI for such a goal. If the auroras expand to too low latitudes and populate the SDI FoV, neutral wind variations seen by HRP SDI would be more pertinent to auroral dynamics than to subauroral processes, and STEVE, even if existing, could be out of the FoV of GAKO ASI. Therefore, for the above technical reasons we exclude events when the main auroral oval is driven to, and persistently (>30 min) stays at, very low latitudes (<62° MLAT). Such a criterion bars some intense storm/substorm events in which auroras expand substantially equatorward, as we shall address later in this section
5. Gallardo-Lacourt et al. (2018b) found that STEVE may have a longitudinal extent of ~2,145 km, or ~2.5 h MLT assuming an average latitude of ~60°. A similar conclusion was also reached in Nishimura

et al. (2020c). Since the available wind data are from PKR/HRP SDIs (∼−90° MLON), our search for the optical signature of STEVE is limited to ASIs in Alaska and western Canadian sectors, with Athabasca (∼−52° MLON, see Figure 1) the eastern-most ASI station to be considered. It is possible that STEVE may exist in further eastern sectors (e.g., February 8, 2016 event to be presented later in this section), but such a case may not invalidate our research goal, namely the possible effects of neutral winds on the local existence/nonexistence of STEVE

Over 2010–2012, we have identified 10 events that meet the above criteria. Their neutral wind variations observed by HRP SDI from substorm onset to 1.5 h after are presented in Figures 10–12. This time range is based upon Gallardo-Lacourt et al. (2018b)'s finding that, the emergence of STEVE usually lags the substorm onset by ∼50–80 min. Any neutral wind variations that might contribute to the rise of STEVE should presumably transpire and sustain for a while before the latter, and thus should have occurred no much beyond ∼1 h after the onset. In most of the events, the temporal resolution of the SDI measurements is ∼2–4 min which suffices for our research purpose. There are a few events (event F/G, and partly in event I/J) in which the SDI at times runs in a low-resolution mode, so that large gaps (∼13–14 min) may exist among the data. Such data gaps do not significantly affect our evaluation of the overall wind variation pattern after substorm onset, but the wind divergence calculation during these gaps would be missing, adding uncertainty to our evaluation of the maximum wind convergence (see later in this subsection and Figure 14d) in those events. The minimum AL in each event reached in each event ranges between ∼ −250 and −700 nT, weaker than the two STEVE events reported abut not systematically different from the overall AL range of STEVE occurrence (Gallardo-Lacourt et al., 2018b). An intense substorm (AL ∼ −950 nT) from Zou et al. (2020)'s events will be separately introduced later in this subsection.

Each subfigure in Figures 10–12 denotes one event, which is indexed to facilitate reference. For each event subfigure, the top panel gives the auroral keogram from the GAKO THEMIS ASI. In the second and third panels we plot the keogram of the east-west wind and the north-south wind from HRP SDI data using the same procedure as for the STEVE events. The neutral wind velocities in all events are plotted in the same color scheme as that in the two STEVE events, to facilitate a cross-comparison. On top of each event subfigure we also show the minimum AL index reached during the substorm, as a proxy of the substorm strength. In the bottom panel of each subfigure we show the wind divergence within two latitudinal ranges: ∼61°-62.5° (green) and 62.5°-64° MLAT (black), calculated from the procedure introduced in Section 3.1. The latitude width used in the divergence calculation is the same as that for the two STEVE events, designed to accommodate enough (>10 as our criteria) data points to ensure numerical reliability in a least squares fitting against instrumental noise and occasionally bad data points. The PKR SDI data are not presented here but are involved in the calculation of the wind divergence. Note that Event F has no PKR data available, but in this event the winds are dominantly northward. The pattern is outright opposed to that in STEVE cases, so that the wind convergence is not important for our arguments and thus not calculated there. We emphasize again that we intend to compare the subauroral neutral wind pattern during nonSTEVE events with that during STEVE events. Occasionally in some events, there may be some hints of wind divergence at >64° MLAT (e.g., event H/J, and see Figure 13 later), but they occur at auroral latitudes (see top panel) and are not much relevant to our research interest. STEVE is never found to occur at >64° MLAT to the authors' recognition, while latitudes at <61° MLAT contain insufficient data points for a reliable computation of wind divergence from our algorithm. Therefore, the latitude ranges in which we calculate the wind divergence is delimited between 61° and 64° MLAT. Such a range covers the latitudes of initial STEVE emergence in many realistic STEVE events according to the existing literature (e.g., Gallardo-Lacourt et al. [2018b]) and our experience. It is true that STEVE might at times occur at even lower latitudes (e.g., <60° MALT), but identification of the existence/nonexistence of those lower-latitude STEVEs and their possible relationship with neutral winds is beyond the instrumental and methodological capability of this study.

A westward wind enhancement after substorm onset is seen in most but not all nonSTEVE events. Since the local time sector of interest is close to the dusk, an eastward wind led by the day-night temperature difference is expected and indeed often seen, particularly at lower latitudes. The westward wind intensification is presumably contingent upon the strength of the substorm-related SAPS and its competence with the ambient eastward wind. The meridional wind is more of interest in this study. In some of the events (event B/C/F/I), mainly northward winds mixed with some sporadic weak equatorward winds prevail in ∼1 h after

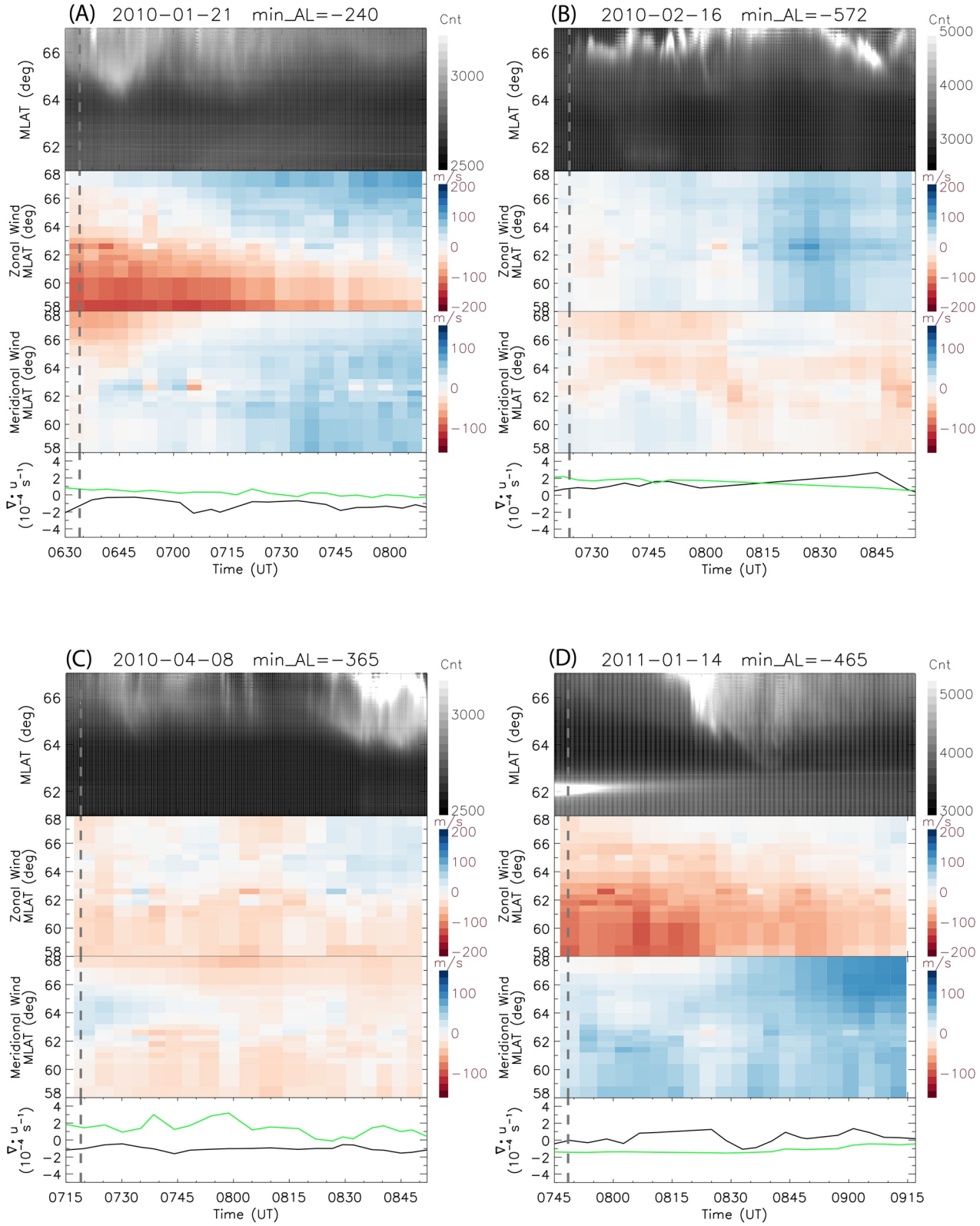

Figure 10. Each subfigure represents one nonSTEVE substorm event. In each subfigure, the top panel shows the ASI keogram sampled along the center meridian of HRP based on 110 km emission height. The second and third panels are the keogram of the east-west wind and the north-south wind from HRP 630 nm SDI. The bottom panel shows the calculated wind divergence at 62.5°-64° MLAT (black) and 61°-62.5° MLAT (green). The substorm onset time is marked by a vertical dashed line.

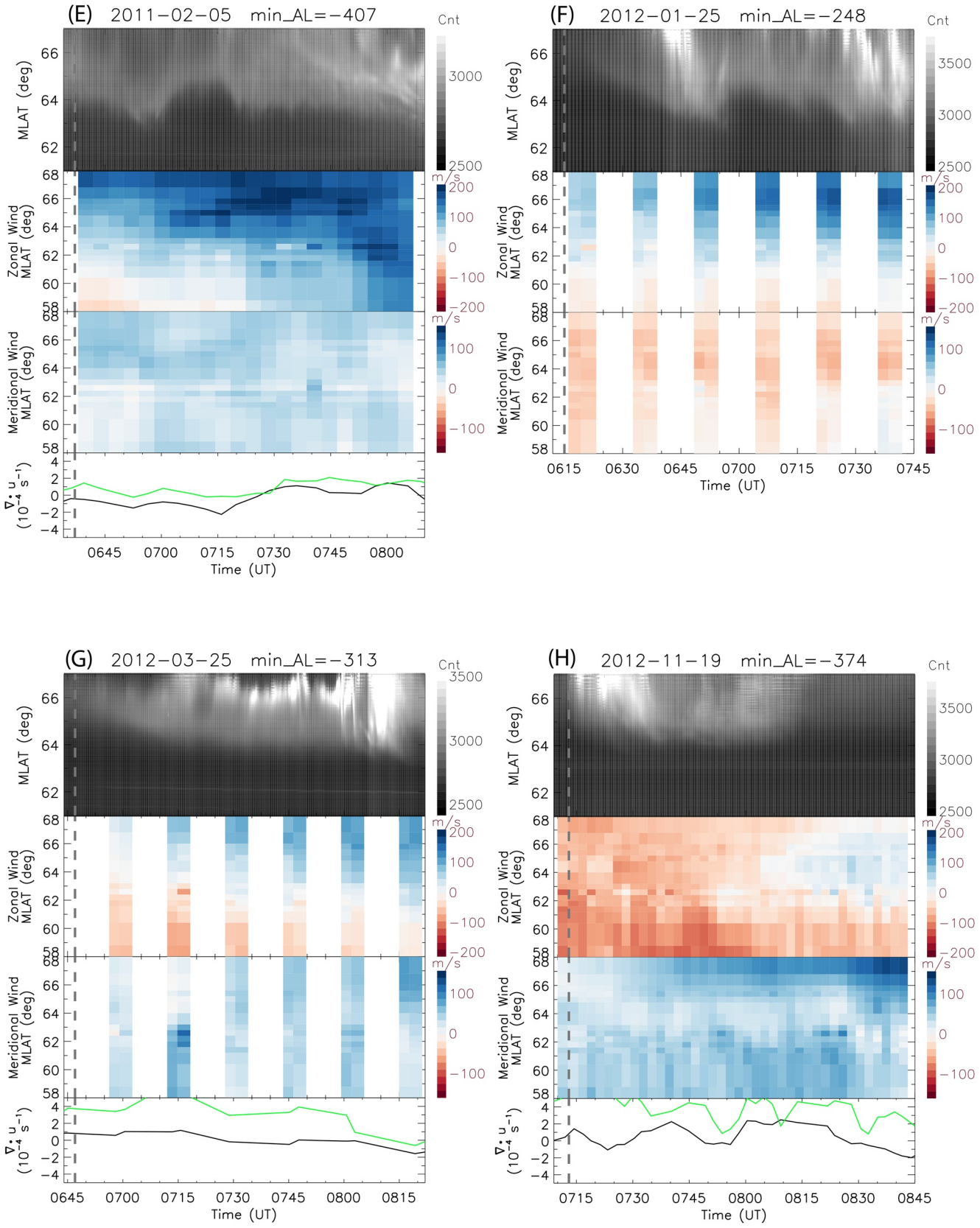

Figure 11. A continuation of Figure 10.

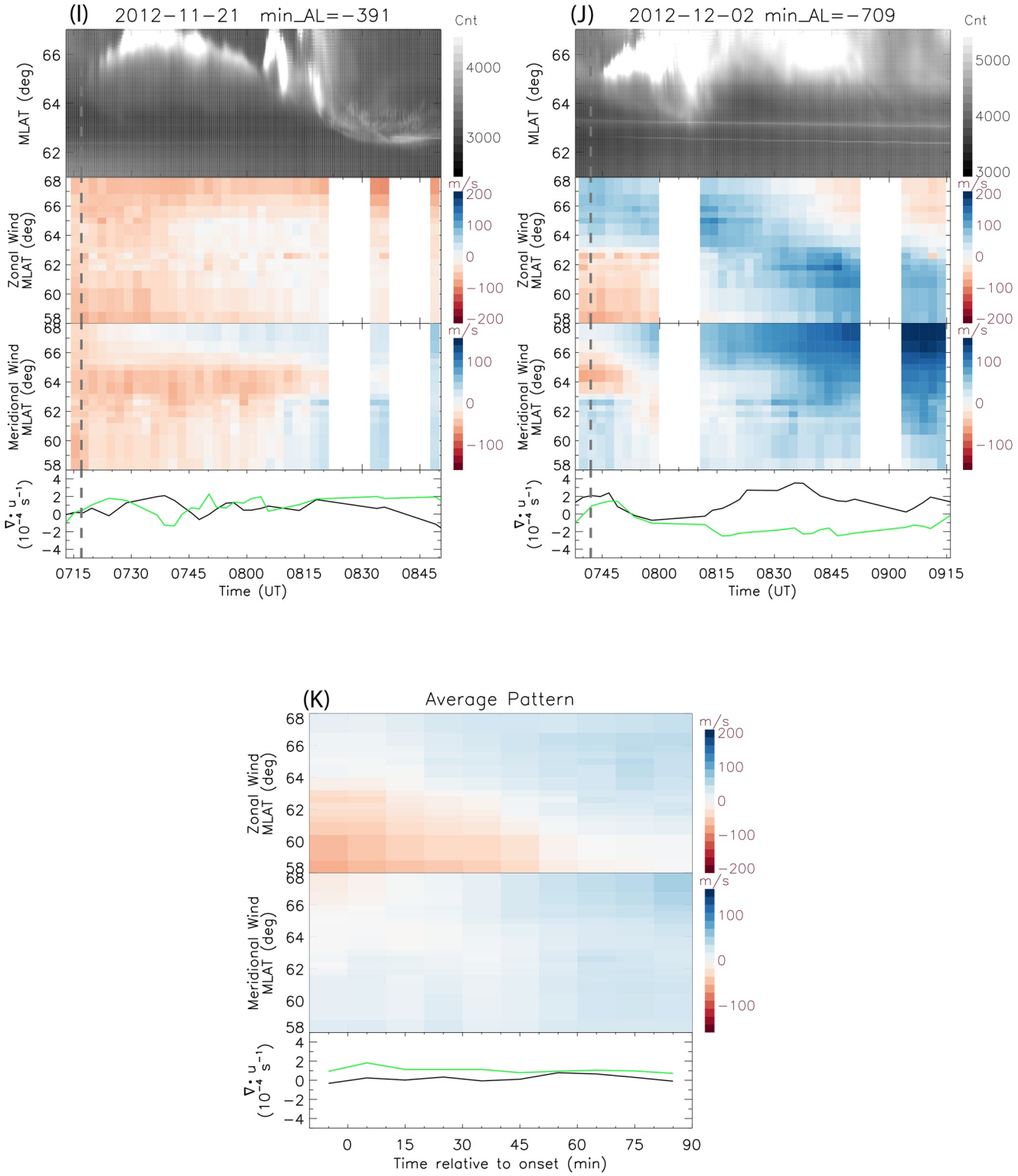

Figure 12. A continuation of Figures 10 and 11. (k) shows the averaged keogram of zonal and meridional winds, as well as the averaged wind divergence, according to time relative to substorm onset.

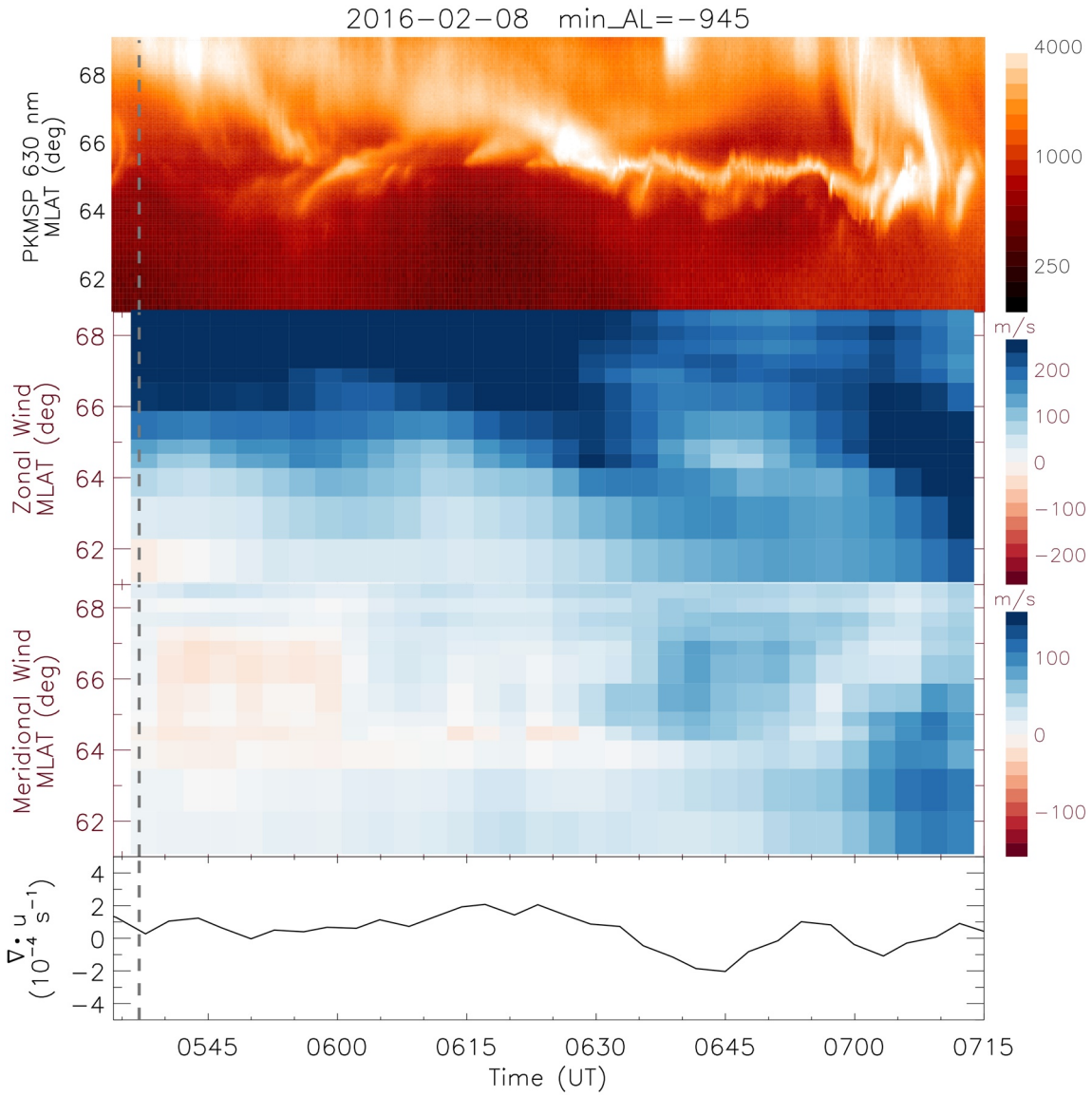

Figure 13. The top panel shows the 630 nm auroras observed by PKR MSP on February 8, 2016 based on 230 km emission height. The second and third panels show the east-west and north-south components of the neutral wind velocity observed by PKR 630 nm SDI. The bottom panel shows the calculated wind divergence at 62.5°-64° MLAT.

onset. This is compatible with Zou et al. (2020)'s result that, a southward wind intensification after substorm onset is not found as statistically prevailing in the evening sector. In those events with perceptible southward wind intensification, except for few events (event D/J) the intensifications at the transition latitude (~64°-65° MLAT) from auroral to subauroral regions tend to be about ~25%–50% weaker than that achieved in the STEVE events. At subauroral latitudes (<~64° MLAT) of interest, the southward winds in general appear to extend well into low latitudes. There are occasionally singular gaps/blanks among the data due to bad/missing data points, but there is little sign of systematic and long-standing (>10 min) manifestation of "stop latitude" as in STEVE events. The wind convergence calculated in the 61°-62.5° and 62.5°-64° MLAT ranges seldom exceeds $\sim 2 \times 10^{-4}\,s^{-1}$. One event that somehow resembles the STEVE events in terms of neutral wind variations is event J. The southward wind intensification is strong—we however footnote that, as compared to the two STEVE events the local time of observation in event J is closer to midnight, where both the ambient trend and substorm-associated components of the southward winds are supposedly stronger (Emmert et al., 2006; Zou et al., 2020). There appears to be a gradually decreasing trend of southward winds

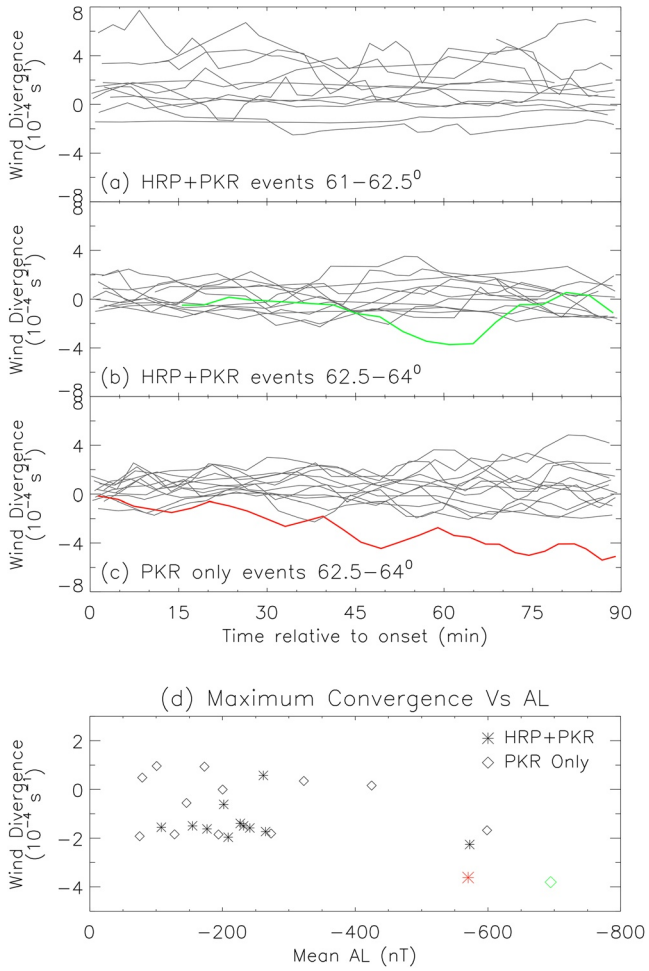

Figure 14. (a) Calculated wind divergence in 61°-62.5° MLAT, superimposed according to the time relative to substorm onset from 13 HRP + PKR events. (b) same as (a) but for 62.5°-64° MLAT. (c) same as (b) but for 13 PKR-only events. The two STEVE events are highlighted in color in (b and c). (d) The minimum wind divergence reached in each event, versus the mean AL averaged in 0–30 min before the minimum divergence epoch. Asterisks and diamonds denote HRP + PKR events and PKR-only events, respectively.

toward lower latitudes during ~08:30–08:50 UT in this event, but the decreasing slope is less abrupt and, the wind convergence is weaker there (up to ~2.4×10^{-4} s^{-1}) than in STEVE events.

Figure 12k shows the averaged keogram of zonal and meridional winds, as well as the averaged wind divergence in the two subauroral latitude ranges, for the 10 collected events. In the data processing we have averaged/interpolated the data to ten 10-min bins spanning from −10 to 90 min relative to onset. There is a perceptible trend of westward wind intensification after the substorm onset, which subsequently progresses southward. There also seems to be a subtle enhancement of southward winds at auroral latitudes after the onset. We however remind that an enhancement toward ~90 min after the onset, when the substorm itself has subsidized in most of our events, could be at least partly attributed to an ambient diurnal trend, namely that neutral winds tend to become more southward when approaching local midnight (Emmert et al., 2006; Zou et al., 2020). At subauroral latitudes, the meridional winds are weak and seem to be more or less constant or slowly vary across latitudes, and the wind divergence there is tiny or even positive on average.

Our analyses are supplemented by the premidnight event pool in Zou et al. (2020), who independently surveyed substorm events with SDI measurements from late 2012 to 2017, though their main research interest is at auroral latitudes. They also stipulate that AL < −200 nT must be reached for the substorms chosen, but they did not check optical data and did not distinguish STEVE or nonSTEVE events. Most of their events (13 out of 15) have only PKR SDI observations, without GAKO THEMIS ASI and HRP SDI data, since the latter two instruments both ceased operation in early 2014. However, we have checked other available THEMIS ASI observations in Alaska and western Canada sectors (up to Athabasca ASI, see afore-mentioned event criterion 5) found no evidence of STEVE in available ASI data for those events. Also, digital all-sky-camera data at GAKO run by the University of Alaska at Fairbanks are available in five of Zou et al.'s events after 2016, and in none of them any visible signature of STEVE is found. While Zou et al.'s events are not ideal in distinguishing the existence or nonexistence of STEVE, they may nevertheless be useful in providing complementary information on the wind convergence at subauroral latitudes during substorm intervals as well as its possible dependence on the substorm intensity. Upon checking available optical data we exclude February 17, 2017 event, in which the auroras are found to extend to very low latitudes (~62° MLAT), in the following analyses as per our criterion (4).

We exemplify one such PKR-only event in Figure 13. This February 8, 2016 event represents an intense substorm: its AL reaches ~950 nT which is even stronger than the two reported STEVE events. Note that in this event STEVE was seen on the Lucky Lake (~59.1° MLAT, −42.5° MLON) red-line imager (data available at https://data.phys.ucalgary.ca/sort_by_project/GO-Canada/), which is more than 3 h MLT east and 4° MLAT south to the GAKO station, after ~06:45 UT. However, no STEVE is visible in the observations from the GAKO digital all-sky-camera (not shown, data available at ftp://optics.gi.alaska.edu/GAK/DASC/) and the Whitehorse (WHIT) THEMIS ASI. Even if the STEVE did extend over ~3 h MLT into Alaska sector, it was likely situated at lower latitudes beyond the FoV of GAKO/WHIT cameras and PKR SDI. With such a possibility in mind, the event may be better depicted as a "local nonSTEVE event," within the latitude/MLT scope of available observations. That said, we argue that the event may still be suitable for our research objective to study the potential role of neutral winds on the local existence/nonexistence of STEVE. The top panel of Figure 13 shows the 630 nm emissions derived from PKR MSP observations. The second and third

panels show the zonal wind and the meridional wind observed by PKR SDI. Accompanying each auroral equatorward expansion at ~05:50, ~06:25, and ~07:00 UT, there is an equatorward propagating trend of intense westward winds. The southward winds are however, not as strongly intensified. They remain very weak during the first auroral expansion, and are moderately intensified for the second auroral expansion, but the enhanced southward winds are essentially confined to >64° MLAT, that is, mostly within auroral latitudes. They seem not to penetrate well into subauroral latitudes. We however cannot entirely rule out the possibility of the LOS integral effect as one contributing cause of the diminishing winds at lower latitudes, which is a potential issue for the PKR-only events. For the third and strongest auroral intensification and expansion after 06:50 UT, the southward winds enhanced accordingly and penetrated down to the equatorward edge of the PKR SDI FoV, yet without any evident sign of a stop latitude. To summarize the observations, the southward winds either do not appear to enter subauroral latitudes, or do not have a distinct stop latitude in the subauroral region. The bottom panel of Figure 13 shows the wind divergence calculated in the latitude range 62.5°-64° MLAT using the procedure described in Section 3.2. As one can see, though this substorm is stronger, the wind divergence is noticeably weaker than that in the STEVE events.

We calculate the wind divergence for all Zou et al. (2020)'s premidnight events. For the two events with PKR and HRP SDI data, we apply the algorithm described in Section 3.1 in two latitudinal ranges: 61°-62.5° and 62.5°-64° MLAT. Together with April 4, 2010 STEVE event and nine nonSTEVE events from the survey in this study (event F has no PKR SDI data), there are 12 HRP + PKR events in total. The other 12 events from Zou et al. (2020) only have PKR SDI data; we adopt the method described in Section 3.2. Note that for those PKR-only events we can only calculate the divergence in 62.5°-64° MLAT, since the 61°-62.5° latitude range has insufficient (three within ±3° MLON of the PKR center meridian) PKR data points for a reliable fitting. Figures 14a–14c give the plots of the calculated wind divergence superimposed according to the time relative to the substorm onset, from 12 HRP + PKR events and 13 PKR-only events (including the March 26, 2008 STEVE event), respectively. The two STEVE events (both occurring at ~63° MLAT) are highlighted in color in Figures 14b and14c. It can be seen that, in STEVE events the wind convergence reaches outlier values that are rare in any other substorms we have investigated. This indicates that a strong wind convergence is not a common feature in normal substorm events.

One may wonder that the STEVE events feature stronger wind convergence simply because their underlying substorm strength is stronger than that in nonSTEVE events. A counterexample in this regard has been given in Figure 13. To further investigate this, we identify the maximum convergence (in terms of average over sliding 10-min windows) reached in each event, and then calculate the mean AL averaged over the interval 0–30 min before the maximum convergence epoch. In doing so we have taken into consideration the typical ion-neutral coupling timescale (Nishimura et al., 2020b). For the HRP + PKR event, the maximum convergence is determined as the larger one found in the two latitude ranges, while for the PKR-only events the convergence is only calculated in the 62.5°-64° MLAT range. The outcome is shown in Figure 14d. Results from two STEVE events are highlighted in color. There might be a vague trend of increasing wind convergence with the substorm intensity, but such a trend is slim to say the best. For the nonSTEVE events, the maximum convergence is no more than $\sim 2 \times 10^{-4}$ s^{-1}, regardless of the substorm intensity, while in STEVE events the wind convergence stands out with outlier values. However, we admit that there is a relative scarcity of intense substorms, particularly in the event pool collected in this paper with HRP SDI data. One of the reasons for the lack of intense substorm events is due to our criteria (4): since we aim to study subauroral wind dynamics with HRP SDI, we have ruled out events when a main portion of the SDI FoV is immersed in auroras, which is often the case under very strong substorms. Based upon available events, we are unable to firmly answer the inquiry that, whether the wind convergence at subauroral latitudes would tend to occur more often and be stronger when the substorm is sufficiently intense. This shall be left for future studies, ideally with SDI/ASI measurements at more equatorward latitudes. We footnote that a related question that whether the STEVE occurrence is statistically biased toward more intense substorms is not firmly answered to date either.

To summarize, from a survey of nonSTEVE substorm events and a comparison with STEVE events, we find that the southward wind intensifications tend to be in general weaker in nonSTEVE events. In some of the nonSTEVE events, the winds at subauroral latitudes remain mainly northward. For the rest of events with southward wind intensification after substorm onset, there is in general no well-defined signature of a stop

latitude of southward winds at subauroral latitudes, and the wind convergence calculated at subauroral latitudes is found to be consistently weaker than that in STEVE events.

4. Discussions

In this study, we investigate the patterns and variations of the neutral wind and temperature from the substorm onset to the STEVE emergence. Some of the observed variations can be understood in the context of the substorm auroral intensification and the subsequent development of SAPS flows equatorward of the intensified auroras as a part of the Harang system (e.g., Nishimura et al., 2008; Zou et al., 2009, 2012). The SAPS flows impose two important influences on the neutral winds: (1) the intensification of westward winds via ion drag and (2) the neutral temperature enhancement via Joule heating. An equatorward wind may arise due to a combined effect of ion drag led by equatorward plasma flows and a poleward pressure gradient associated with the SAPS-related Joule heating. The westward and southward wind intensifications are evident and relatively strong in STEVE events. However, in a survey Zou et al. (2020) found that southward wind intensifications are not statistically prevailing in the premidnight sector during normal substorms (they did not distinguish STEVE and nonSTEVE events). We also notice from our survey that, the winds are dominantly northward in some nonSTEVE events and are only moderately enhanced in some other events. It thus appears that the southward wind intensification tends to be more pronounced in STEVE events than in a majority of nonSTEVE events. While the overall substorm strength is likely one potential factor controlling the thermospheric response, one other possible reason underlying the different wind variations during STEVE and nonSTEVE events might be the duskward extension of the magnetospheric energy input. In a recent study Nishimura et al. (2020c) suggested that magnetosphere injection and convection configurations are more skewed to premidnight during STEVE intervals. For the local time range under investigation in this study, the GAKO sector is close to dusk. The substorm disturbance usually originates east of Alaska and then propagated westward. In this regard we have checked the magnetometer and auroral (mosaic movie available at https://data-portal.phys.ucalgary.ca/themis/mosaic_movies) data and notice that, during both two STEVE events reported in this paper, the substorm bulge well extends to Alaska before STEVE emergence, and thus the level of magnetospheric energy input in the STEVE region was presumably larger. On the other hand, in some of the nonSTEVE events, while the substorm activity does reach Alaska, that is, in the form of arc intensifications, a full-fledged substorm bulge is not always extended to and well established in the GAKO sector. A larger magnetospheric energy input at premidnight due to an extended bulge activity for the STEVE events may potentially lead to a stronger thermosphere response in the STEVE occurrence region (Nishimura et al., 2020c).

Another interesting finding in this study lies in that, the intensified equatorward winds in STEVE events appear to feature a stop/reversal at certain latitude, and strong wind convergence (~4–5 × 10^{-4} s^{-1}) is developed there. This pattern sustains for ~15–20 min, and then STEVE arises at about this stop latitude. We remind that, to ensure the numerical reliability in a least squares fitting against the instrumental noise and the uncertainty led by u_z, the wind divergence is computed over a latitude width (1.5° MLAT) much wider than the STEVE arc (0.1°-0.2° MLAT). In comparison, an evident stop latitude of southward winds is not as well seen, and the calculated convergence at subauroral latitudes is consistently smaller, in nonSTEVE events. From the achieved results in this study we are able to claim that a strong wind convergence is not a common feature during normal substorm intervals at subauroral latitudes in the evening sector of interest. That said, since there are inadequate intense substorms in our event pool, we are unable to determine in this study whether the wind convergence would occur more often and be stronger when the substorm is sufficiently intense. Anyway, we emphasize that we only hypothesize the strong wind convergence as one contributing factor, not a sufficient condition, for STEVE to occur, as we shall elucidate later in this section.

In the following, we shall discuss the potential implication of our findings to the possible mechanism of STEVE production. One of the most striking features of STEVE is that it contains an overall enhancement of a continuous spectrum as its main source of brightness (Gillies et al., 2019; Liang et al., 2019). The most likely source of such AGC is a certain kind of chemiluminescence. Several potential mechanisms of the AGC are being investigated by the authors and colleagues, but one of the leading difficulties in these interpretation efforts lies in that, the observed optical intensity of STEVE summons a high concentration of relevant neutral constituents (including their excited states) involved in the chemiluminescence. In contrast,

many of the key relevant constituents (such as NO, N (^{2}D, ^{4}S), and excited N_2 in a NO_2 continuum scenario) are supposed to have a low concentration in the nightside subauroral region in absence of electron precipitation. We propose that the transport effects led by neutral winds might partly help solve this dilemma. More specifically in terms of our observations: (1) Enhanced equatorward neutral winds can transport relevant neutrals species, which are excited by auroral precipitations and may have crucial importance in the airglow production, to subauroral latitudes (Solomon et al., 1999; Vlasov & Kelley, 2003). (2) Furthermore, the neutrals may pile up due to the wind convergence, potentially leading to an enhancement of their densities. It should be noted that the gas continuity equation is inherently coupled with the momentum equation, such that the relationship between the neutral density variation and the wind divergence is complex. Dhadly et al. (2015) suggested that the thermosphere is largely convectively stable. Their argument is based on the consideration that the density and pressure changes led by the wind divergence would oppose the original divergence/convergence that produced them. While this may be true for the major neutral species (e.g., atomic oxygen in the upper thermosphere), we argue that minor neutral species (including excited-state neutrals) would be more passive to the neutral wind variations set up by external pressure gradients, since those constituents have minor only contributions to the total pressure. There is also a possibility that the horizontal wind divergence may be balanced by the vertical transport term $\nabla\cdot\left(n\boldsymbol{u}_z\right)$. In the afore-addressed context that westward/southward wind enhancement and T_n intensification originating from auroral latitudes are related to SAPS and its resulting Joule heating, one would also expect a substantial neutral upwelling, which acts to lift the molecule-rich air from lower to higher altitudes and change the neutral composition there (e.g., Wang et al., 2012; Zhang et al., 2014). SDI observations cannot yield the distribution and height profile of the vertical wind. In April 4, 2010 event, u_z given by the HRP zenith data point is small (<20 m/s, not shown) and mostly downward during the interval of strong horizontal wind convergence. We have also tried the bistatic method in Anderson et al. (2012b) to derive u_z for this event. While unfortunately the common-volume locations suitable for the Anderson et al. (2012b) u_z analysis (see their Figure 1) are all at ≥∼64° MLAT and thus not in the subauroral region of our core interest, the derived u_z pattern at those locations (not shown) are found to be semi-quantitatively similar to that inferred from the HRP zenith data point. If such a pattern is assumed as the general pattern of u_z at the SDI observation height (∼250 km), one may imagine that the upwelling from the lower thermosphere might lead to the convergence of molecular air at certain altitudes. Though the lack of definite u_z observations inevitably brings uncertainty, we argue that there seems to be no straightforward rationale to conceive that the vertical transport term $\nabla\cdot\left(n\boldsymbol{u}_z\right)$ would necessarily act to cancel, if not to reinforce, the convergence of some molecular air constituents. Combining the above thoughts, it is not unreasonable to conceive that at least some neutral constituents might undergo substantial pileup due to the observed wind convergence.

Of course, we are not to claim that the neutral pileup led by neutral winds may itself be sufficient in solving the afore-mentioned difficulty of chemiluminescence airglow—it certainly cannot. To account for the drastic increase of the STEVE airglow brightness, an external energy source must be involved. Based upon the current knowledge of STEVE, the SAID becomes the topmost candidate for such an energy source. SAID is similar to SAPS in a number of aspects (some researchers consider SAID as a subclass of SAPS), but is usually characterized by somehow stronger flow magnitude and narrower latitudinal width (Anderson & Landry, 2017; Mishin et al., 2017). Elevated electron temperature and depleted electron density are typically observed within the SAID channel (e.g., Archer et al.,2018, 2019a; Moffett et al., 1998; Spiro et al., 1979). STEVE is found to be co-located with such a SAID channel in joint optical and in situ satellite observations (Archer et al., 2019a; Chu et al., 2019; MacDonald et al., 2018; Nishimura et al., 2019). Nishimura et al. (2020c) suggested that substorms and particle injection extending far duskward away from midnight offer a condition for creating SAID and STEVE due to stronger electron injection to premidnight. Some of the STEVE features, such as the narrow latitudinal width and especially its fast westward propagation, are likely pertinent to SAID characteristics. In both of our STEVE events, the STEVE shows a westward expansion: it appears first near the eastern edge of the GAKO ASI FoV and then progressively expands westward. The westward expansion speed is evaluated as ∼3–5 km/s, which is compatible with the typical STEVE-related SAID velocity (Archer et al., 2019a).

The exceptionally high ion kinetic energy and electron temperature characteristic of SAID open new possibilities of chemiluminescence airglow processes. We shall use the NO_2 continuum ($NO + O \rightarrow NO_2 + h\nu$)

as an illustrational example. Classical views of the NO production in the nightside thermosphere usually focus on the following reaction (e.g., Barth et al. 2003, 2009; Lin et al., 2018),

$$N + O_2 \rightarrow NO + O \quad \text{(R1)}$$

which has a low activation barrier (~0.27 eV) and thus may occur regularly under normal thermosphere conditions (e.g., with N (^{2}D) participating). However, a major problem of R1 lies in that, even under a steady-state limit, the resultant NO concentration can only be no more than ~0.1 (O_2) (Hyman et al., 1976). It is unlikely that the reaction R1 could be capable of producing enough NO and in turn the NO_2 continuum yield to account for the observed STEVE AGC brightness (Gillies et al., 2019; Liang et al., 2019). The other reaction

$$N_2 + O \rightarrow NO + N \quad \text{(R2)}$$

has an activation barrier of ~3.27 eV. To overcome this energy barrier, an electronically excited state of N_2 or O, or a higher-order vibrationally excited state of N_2 is required. More specially, for vibrationally excited N_2 $v' > 11$ is needed if reacting with ground-state O (^{3}P), or $v' > 4$ if reacting with O (^{1}D), which is known to exist based upon the 630 nm red-line component of STEVE (Gillies et al., 2019; Liang et al., 2019; MacDonald et al., 2018). Despite the energy barrier, the reaction R2 can potentially yield higher rates of NO production than R1 (Harding et al., 2020), and was thus at times invoked in attempts to explain the exceptionally high NO densities in certain observations (e.g., Zipf et al., 1970). In the presence of a strong SAID, N_2 molecules are indeed prone to be excited to higher vibrational levels due to the very high electron temperature (Newton et al., 1974), and/or via nonreactive collisions with fast-streaming ions (Harding et al., 2020). Still, the model is contingent upon the local ambient N_2 density. To be capable of producing the realistic STEVE brightness, a substantial increase of the N_2 density in the >150 km thermosphere was premised in Harding et al. (2020), which in their 1D model was assumed to be led by the hydrostatic expansion/upwelling of the atmosphere under SAID-related heating (e.g., Wang et al., 2012). While such neutral upwelling might indeed occur, we suggest that the horizontal wind convergence may serve as one other effective way to help N_2 density buildup. Furthermore, as afore-mentioned, the neutral winds may act to transport the vibrationally excited N_2 from the auroral region and pileup at subauroral latitudes. Note that such a transport process was invoked by Vlasov and Kelley (2003) to explain the formation of the electron trough in the subauroral region. The vibrationally excited N2 typically has much longer lifetime in the upper thermosphere (~hours, see Vlasov and Kelley [2003]) due to the reduced collisional deexcitation with O. When they are transported into the SAID channel, they may undergo excited-to-excited transitions between different vibrational levels (Newton et al., 1974), and thus may further populate the higher-level vibrational states of N_2. To summarize, when the above transport processes of excited N_2 of auroral origin are considered, the generation of NO via reaction R2 would be more effective and productive than that evaluated in Harding et al. (2020). At last, we mention that the neutral winds may also directly help the transport and pileup of auroral precipitation-induced NO at subauroral latitudes (e.g., Solomon et al., 1999).

While our above discussion is mostly built upon a premise that the NO_2 AGC contributes to the STEVE AGC, the essence of our proposal might also be applicable to other possible mechanisms of the chemiluminescence AGC. In short, the presence of SAID, along with its exceptionally high electric field, ion kinetic energy, and electron temperature, serves as the energy source for STEVE to occur, while a transport and pileup effect led by the neutral wind variations may prepare a reservoir of relevant neutral constituents and in turn enhance the production rate and the resultant airglow yield. We thus speculate that STEVE is more readily to transpire under a coincidental circumstance that the buildup of neutrals occurs around at the same latitude as SAID (though the former may have a somewhat wider latitudinal scale). This may partly explain the fact that only a subset of SAIDs is found to be accompanied by STEVE, even with conjunctive optical observations (Archer et al., 2019a; Nishimura et al., 2020a). One example in our event pool is the February 16, 2010 event (event B in Figure 10; DMSP data are studied by Nishimura et al. [2020a]). Despite being a relatively strong substorm (AL ~ −570) no equatorward wind transport or divergence is found at subauroral latitudes. DMSP F18 crossed a SAID channel at ~08:06 UT (though in the southern hemisphere), but in its conjugate Alaska sector in the northern hemisphere, no clue of STEVE was found in optical data.

Admittedly, the above proposal remains tentative and somehow hypothetical at the current stage. We emphasize again that STEVE is a fairly new phenomenon, and its generation mechanisms remain poorly understood to date. This paper presents an initial study to address the possible role of neutral dynamics in STEVE production. To carry on this study, we are to collect more STEVE events with neutral measurements, from both ground-based instruments and in situ satellites, in the future. We are also working on a global MIT simulation to model the neutral density/temperature/wind variations during substorm intervals and in the presence of strong SAPS/SAID. Through these studies, we look forward to gaining a better understanding of the neutral dynamics and its potential contribution to STEVE production in the future.

5. Conclusions

In this study, we make an initial effort to investigate the potential preconditioning role of neutral dynamics in STEVE production. Using joint SDI and optical ASI observations, we study the pattern and variations of the neutral wind after the substorm onset but before the STEVE emergence, and compare with that in nonSTEVE events. Neutral winds enhance in westward and southward directions following substorm auroral intensification, and show equatorward propagating trend originating from auroral latitudes. However, in STEVE events the enhanced equatorward winds appear to feature a stop/reversal at certain subauroral latitude, and strong wind convergence is developed there. This pattern sustains for ~15–20 min, and then STEVE arises at about this stop latitude. Such a stop latitude of equatorward winds and wind convergence are weaker in nonSTEVE events. This is owing partly to that the southward wind intensification from auroral latitudes is in general weaker in nonSTEVE events, and partly to that the southward winds are more liable to penetrate to lower latitudes in nonSTEVE events. The former discrepancy is likely related to the differences in the underlying substorm strength and/or in the duskward extension of the magnetospheric energy input between STEVE and nonSTEVE substorm events (Nishimura et al., 2020c). We speculate that a mid-latitude T_n intensification and its resultant southward temperature gradient, which are indeed observed in STEVE events before the STEVE emergence, might act to impede the southward winds from auroral latitudes and help form the stop latitude of winds, but such a hunch needs to be furthered examined in the future, ideally with more definite T_n observations at mid-latitudes.

Our results may shed some implications on the so-far mysterious production mechanism of STEVE. While there is mounting evidence that the AGC component of STEVE that dominates the overall STEVE brightness (Gillies et al., 2019; Liang et al., 2019), likely stems from certain extremely intensified chemiluminescence in the upper thermosphere, many proposals of the underlying AGC mechanisms are baffled by the requirement of high concentrations of some key neutral continents in subauroral latitudes at STEVE altitudes, to explain the realistic STEVE brightness. We propose that the transport effects led by neutral winds might partly help solve this difficulty. Enhanced equatorward neutral winds can transport relevant neutrals species that are excited by auroral precipitation and have crucial importance in the AGC production to subauroral latitudes. These neutrals may pile up due to the wind convergence at the stop latitude of the equatorward winds. Such a transport and pileup effect led by the neutral wind variations may prepare a reservoir of key neutral constituents. When SAID passes through, due to its high ion kinetic energy and electron temperature the SAID would actively interact with the enhanced concentrations of relevant neutrals there (e.g., Harding et al., 2020), leading to a dramatic increase of the airglow production and the STEVE occurrence.

Data Availability Statement

SDI data are available at http://sdi_server.gi.alaska.edu/sdiweb. PFISR data are available from http://isr.sri.com/madrigal. We thank the help of Dr. Donald Hampton in processing the DASC data at GAKO and MSP data at PKR (available at http://optics.gi.alaska.edu/optics) for some events. We also gratefully acknowledge the SuperMAG collaborators. We thank for enlightening discussions with Dr. Brian Harding, Dr. J.-P. St. Maurice, and Dr. Yongliang Zhang.

Acknowledgments
This work is supported by the Canadian Space Agency. Dr. Ying Zou acknowledges support from the NSF grant AGS-1502436. The THEMIS mission is supported by NASA, and data are available at https://themis.ssl.berkeley.edu/index.shtml.

References

Anderson, C., Conde, M., & McHarg, M. G. (2012a). Neutral thermospheric dynamics observed with two scanning Doppler imagers: 1. Monostatic and bistatic winds. *Journal of Geophysical Research: Space Physics*, *117*(A3), A03304. https://doi.org/10.1029/2011JA017041

Anderson, C., Conde, M., & McHarg, M. G. (2012b). Neutral thermospheric dynamics observed with two scanning Doppler imagers: 2. Vertical winds. *Journal of Geophysical Research: Space Physics*, *117*(A3), A03305. https://doi.org/10.1029/2011JA017157

Anderson, P. C., & Landry, R. G. (2017). SAPS and SAID: Differences and implications on modeling. *SA41C-01, paper presented at 2017 Fall Meeting, AGU, New Orleans, 11–15 December*.

Archer, W. E., Gallardo-Lacourt, B., Perry, G. W., St.-Maurice, J.-P., Buchert, S. C., & Donovan, E. F. (2019a). Steve: The optical signature of intense subauroral ion drifts. *Geophysical Research Letters*, *46*(12), 6279–6286. https://doi.org/10.1029/2019GL082687

Archer, W. E., & Knudsen, D. J. (2018). Distinguishing subauroral ion drifts from Birkeland current boundary flows. *Journal of Geophysical Research: Space Physics*, *123*(1)819–826. https://doi.org/10.1002/2017JA024577

Archer, W. E., St.-Maurice, J.-P., Gallardo-Lacourt, B., Perry, G. W., Cully, C. M., Donovan, E., et al. (2019b). The vertical distribution of the optical emissions of a Steve and Picket Fence event. *Geophysical Research Letters*, *46*(19), 10719–10725. https://doi.org/10.1029/2019GL084473

Baker, K. B., & Wing, S. (1989), A new magnetic coordinate system for conjugate studies at high latitudes. *Journal of Geophysical Research*, *94*(A7), 9139–9143. https://doi.org/10.1029/JA094iA07p09139

Barbier, D., Dufay, J., & Williams, D. (1951). Recherches sur l'émission de la raie verte de la lumière du ciel nocturne. *Annual Review of Astrophysics*, *2*(28), 399–437.

Barth, C. A., Lu, G, & Roble, R. G. (2009). Joule heating and nitric oxide in the thermosphere. *Journal of Geophysical Research*, *114*(A5), A05301. https://doi.org/10.1029/2008JA013765

Barth, C. A., Mankoff, K. D., Bailey, S. M., & Solomon, S. C. (2003). Global observations of nitric oxide in the thermosphere. *Journal of Geophysical Research*, *108*(A1), 1027. https://doi.org/10.1029/2002JA009458

Cai, L., Oyama, S.-I., Aikio, A., Vanhamäki, H., & Virtanen, I. (2019). Fabry-Perot interferometer observations of thermospheric horizontal winds during magnetospheric substorms. *Journal of Geophysical Research: Space Physics*, *124*(5), 3709–3728. https://doi.org/10.1029/2018JA026241

Campbell, L., Cartwright, D. C., & Brunger, M. J. (2007). Role of excited N_2 in the production of nitric oxide. *Journal of Geophysical Research*, *112*(A8), A08303. https://doi.org/10.1029/2007JA012337

Campbell, L., Cartwright, D. C., Brunger, M. J., & Teubner, P. J. O. (2006). Role of electronic excited N_2 in vibrational excitation of the N_2 ground state at high latitudes. *Journal of Geophysical Research*, *111*(A9), A09317. https://doi.org/10.1029/2005JA011292

Chu, X., Malaspina, D., Gallardo-Lacourt, B., Liang, J., Andersson, L., Ma, Q., et al. (2019). Identifying STEVE's magnetospheric driver using conjugate observations in the magnetosphere and on the ground. *Geophysical Research Letters*, *46*(22), 12665–12674. https://doi.org/10.1029/2019GL082789

Conde, M., & Smith, R. W. (1995). Mapping thermospheric winds in the auroral zone. *Geophysical Research Letters*, *22*(22), 3019–3022. https://doi.org/10.1029/95GL02437

Conde, M., & Smith, R. W. (1998). Spatial structure in the thermospheric horizontal wind above Poker Flat, Alaska, during solar minimum. *Journal of Geophysical Research*, *103*(A5), 9471–9949. https://doi.org/10.1029/97JA03331

Dhadly, M., Emmert, J., Drob, D., Conde, M., Doornbos, E., Shepherd, G., et al. (2017). Seasonal dependence of northern high-latitude upper thermospheric winds: A quiet time climatological study based on ground-based and space-based measurements. *Journal of Geophysical Research: Space Physics*, *122*(2), 2619–2644. https://doi.org/10.1002/2016JA023688

Dhadly, M. S., Emmert, J. T., Drob, D. P., Conde, M. G., Doornbos, E., Shepherd, G. G., et al. (2018). Seasonal dependence of geomagnetic active-time northern high-latitude upper thermospheric winds. *Journal of Geophysical Research: Space Physics*, *123*(1), 739–754. https://doi.org/10.1002/2017JA024715

Dhadly, M. S., Meriwether, J., Conde, M., & Hampton, D. (2015). First ever cross comparison of thermospheric wind measured by narrow- and wide-field optical Doppler spectroscopy. *Journal of Geophysical Research: Space Physics*, *120*(11), 9683–9705. https://doi.org/10.1002/2015JA021316

Donovan, E. F., Mende, S., Jackel, B., Frey, H., Syrjäsuo, M., Voronkov, I., et al. (2006), The THEMIS all-sky imaging array—System design and initial results from the prototype imager, *Journal of Atmospheric and Solar-Terrestrial Physics*, *68*(13), 1472–1487. https://doi.org/10.1016/j.jastp.2005.03.027

Emmert, J. T., Faivre, M. L., Hernandez, G., Jarvis, M. J., Meriwether, J. W., Niciejewski, R. J., et al. (2006). Climatologies of nighttime upper thermospheric winds measured by ground-based Fabry-Perot interferometers during geomagnetically quiet conditions: 1. Local time, latitudinal, seasonal, and solar cycle dependence, *Journal of Geophysical Research*, *111*(A12), A12302. https://doi.org/10.1029/2006JA011948

Gadsden, M., & Marovich, E. (1973). The nightside continuum. *Journal of Atmospheric and Terrestrial Physics*, *35*(9), 1601–1614. https://doi.org/10.1016/0021-9169(73)90179-7

Gallardo-Lacourt, B., Liang, J., Nishimura, Y., & Donovan, E. (2018a). On the origin of STEVE: Particle precipitation or ionospheric skyglow? *Geophysical Research Letters*, *45*(16), 7968–7973. https://doi.org/10.1029/2018GL078509

Gallardo-Lacourt, B., Nishimura, Y., Donovan, E., Gillies, D. M., Perry, G. W., Archer, W. E., et al. (2018b). A statistical analysis of STEVE. *Journal of Geophysical Research: Space Physics*, *123*(11), 9893–9905. https://doi.org/10.1029/2018JA025368

Gallardo-Lacourt, B., Nishimura, Y., Lyons, L. R., Mishin, E. V., Ruohoniemi, J. M., Donovan, E. F., et al. (2017). Influence of auroral streamers on rapid evolution of ionospheric SAPS flows. *Journal of Geophysical Research: Space Physics*, *122*(12), 12406–12420. https://doi.org/10.1002/2017JA024198

Gillies, D. M., Donovan, E., Hampton, D., Liang, J., Connors, M., Nishimura, Y., et al. (2019). First observations from the TREx Spectrograph: The optical spectrum of STEVE and the picket fence phenomena. *Geophysical Research Letters*, *46*(13), 7207–7213. https://doi.org/10.1029/2019GL083272

Gjerloev, J. W. (2012). The SuperMAG data processing technique. *Journal of Geophysical Research: Space Physics*, *117*(A9), A09213. https://doi.org/10.1029/2012JA017683

Harding, B. J., Mende, S. B., Triplett, C. C., & Wu, Y.-J. J. (2020). A mechanism for the STEVE continuum emission. *Geophysical Research Letters*, *47*(7), e2020GL087102. https://doi.org/10.1029/2020GL087102

Hedin, J., Rapp, M., Khaplanov, M., Stegman, J., & Witt, G. (2012). Observations of NO in the upper mesosphere and lower thermosphere during ECOMA 2010. *Annals of Geophysics*, *30*(11), 1611–1621. https://doi.org/10.5194/angeo-30-1611-2012

Heinselman, C. J., & Nicolls, M. J. (2008). A Bayesian approach to electric field and *E*-region neutral wind estimation with the Poker Flat Advanced Modular Incoherent Scatter Radar. *Radio Science*, *43*(5), RS5013. https://doi.org/10.1029/2007RS003805

Hunnekuhl, M., & MacDonald, E. (2019). A citizen science based data package for STEVE phenomenon related subaurora aurora or auroral-like luminous ionospheric structures. *16th European Space Weather Week*. Retrieved from https://register-as.oma.be/esww16/contributions/public/S2-P1/S2-P1-02-HunnekuhlMichael/POSTER1_ESWW.pdf

Hunnekuhl, M., & MacDonald, E. (2020). Early ground-based work by auroral pioneer Carl Størmer on the high-altitude detached subauroral arcs now known as "STEVE". *Space Weather*, *18*(3), e2019SW002384. https://doi.org/10.1029/2019SW002384

Hunnekuhl, M., MacDonald, E., Swanson, B., Theusner, M., Stone, J., Chernenkoff, A., et al. (2019). STEVE phenomenon related subauroral aurora or aurora-like luminous ionospheric structures—Relevant structures, characteristics and correlations with geomagnetic storms derived from a citizen science based data package. *16th European Space Weather Week*. Retrieved from https://register-as.oma.be/esww16/contributions/public/S14-P1/S14-P1-05-HunnekuhlMichael/POSTER2_ESWW.pdf

Hyman, E., Strickland, D. J., Julienne, P. S., & Strobel, D. F. (1976), Auroral NO concentrations? *Journal of Geophysical Research*, *81*(25), 4765–4769.

Kwak, Y. S., & Richmond, A. D. (2014). Dependence of the high-latitude lower thermospheric wind vertical vorticity and horizontal divergence on the interplanetary magnetic field. *Journal of Geophysical Research: Space Physics*, *119*(2), 1356–1368. https://doi.org/10.1002/2013JA019589

Liang, J., Donovan, E., Connors, M., Gillies, D., St-Maurice, J. P., Jackel, B., et al. (2019). Optical spectra and emission altitudes of double-layer STEVE: A case study. *Geophysical Research Letters*, *46*(23), 13630–13639. https://doi.org/10.1029/2019GL085639

Lin, C. Y., Deng, Y., Venkataramani, K., Yonker, J., & Bailey, S. M. (2018). Comparison of the thermospheric nitric oxide emission observations and the GITM simulations: Sensitivity to solar and geomagnetic activities. *Journal of Geophysical Research: Space Physics*, *123*(12), 10239–10253. https://doi.org/10.1029/2018JA025310

Lu, G., Mlynczak, M. G., Hunt, L. A., Woods, T. N., & Roble, R. G. (2010), On the relationship of Joule heating and nitric oxide radiative cooling in the thermosphere. *Journal of Geophysical Research*, *115*(A5), A05306. https://doi.org/10.1029/2009JA014662

Lyons, L. R., Nishimura, Y., Gallardo-Lacourt, B., Nicolls, M. J., Chen, S., Hampton, D. L., et al. (2015). Azimuthal flow bursts in the inner plasma sheet and possible connection with SAPS and plasma sheet earthward flow bursts. *Journal of Geophysical Research: Space Physics*, *120*(6), 5009–5021. https://doi.org/10.1002/2015JA021023

MacDonald, E. A., Donovan, E., Nishimura, Y., Case, N., Gillies, D. M., Gallardo-Lacourt, B., et al. (2018). New science in plain sight: Citizen scientists lead to the discovery of optical structure in the upper atmosphere. *Science Advances*, *4*(3), eaaq0030. https://doi.org/10.1126/sciadv.aaq0030

Mishin, E., Nishimura, Y., & Foster, J. (2017). SAPS/SAID revisited: A causal relation to the substorm current wedge. *Journal of Geophysical Research: Space Physics*, *122*(8), 8516–8535, https://doi.org/10.1002/2017JA024263

Moffett, R. J., Ennis, A. E., Bailey, G. J., Heelis, R. A., & Brace, L. H. (1998). Electron temperatures during rapid subauroral ion drift events. *Annals of Geophysics*, *16*(4), 450–459.

Newton, G. P., Walker, J. C. G., & Meijer, P. H. E. (1974). Vibrationally excited nitrogen in stable auroral red arcs and its effect on ionospheric recombination. *Journal of Geophysical Research*, *79*(25), 3807–3818.

Nishimura, Y., Donovan, E. F., Angelopoulos, V., & Nishitani, N. (2020a). Dynamics of auroral precipitation boundaries associated with STEVE and SAID. *Journal of Geophysical Research: Space Physics*, *125*(8), e2020JA028067. https://doi.org/10.1029/2020JA028067

Nishimura, Y., Gallardo-Lacourt, B., Zou, Y., Mishin, E., Knudsen, D. J., Donovan, E. F., et al (2019). Magnetospheric signatures of STEVE: Implication for the magnetospheric energy source and inter-hemispheric conjugacy. *Geophysical Research Letters*, *46*(11), 5637–5644. https://doi.org/10.1029/2019GL082460

Nishimura, Y., Lyons, L. R., Gabrielse, C., Sivadas, N., Donovan, E. F., Varney, R. H., et al. (2020b). Extreme magnetosphere-ionosphere-thermosphere responses to the 5 April 2010 supersubstorm. *Journal of Geophysical Research: Space Physics*, *125*(4), e2019JA027654. https://doi.org/10.1029/2019JA027654

Nishimura, Y., Wygant, J., Ono, T., Iizima, M., Kumamoto, A., Brautigam, D., & Friedel, R. (2008), SAPS measurements around the magnetic equator by CRRES, *Geophysical Research Letters*, *35*(10), 1–5. https://doi.org/10.1029/2008GL033970

Nishimura, Y., Yang, J., Weygand, J. M., Wang, W., Kosar, B., Donovan, E. F., et al. (2020c). Magnetospheric conditions for STEVE and SAID: Particle injection, substorm surge and field-aligned currents. *Journal of Geophysical Research: Space Physics*, *125*(8), e2020JA027782. https://doi.org/10.1029/2020JA027782

Ritter, P., Lühr, H., & Doornbos, E. (2010. Substorm-related thermospheric density and wind disturbances derived from CHAMP observations. *Annales Geophysicae*, *28*(6), 1207–1220. https://doi.org/10.5194/angeo-28-1207-2010

Solomon, S., Barth, C. A., & Bailey, S. M. (1999). Auroral production of nitric oxide measured by the SNOE satellite. *Geophysical Research Letters*, *26*(9), 1259–1262.

Spiro, R. W., Heelis, R. A., & Hanson, W. B. (1979). Rapid subauroral ion drifts observed by Atmospheric Explorer C. *Geophysical Research Letters*, *6*(8), 657–660.

Sternberg, J. R., & Ingham, M. F. (1972). Observations of the airglow continuum. *Monthly Notices of the Royal Astronomical Society*, *159*(1), 1–20.

Thayer, J. P., & Killeen, T. L. (1991). Vorticity and divergence in the high-latitude upper thermosphere. *Geophysical Research Letters*, *8*(4), 701–704. https://doi.org/10.1029/91GL00131

Wang, W., Talaat, E. R., Burns, A. G., Emery, B., Hsieh, S., Lei, J., & Xu, J. (2012). Thermosphere and ionosphere response to subauroral polarization streams (SAPS): Model simulations. *Journal of Geophysical Research: Space Physics*, *117*(A7), A07301. https://doi.org/10.1029/2012JA017656

Whiter, D. K., Gustavsson, B., Partamies, N., & Sangalli, L. (2013). A new automatic method for estimating the peakauroral emission height from all-sky camera images. *Geoscientific Instrumentation, Methods and Data Systems 2*(1), 131–144. https://doi.org/10.5194/gi-2-131-2013

Vlasov, M. N., & Kelley, M. C. (2003). Modeling of the electron density depletion in the storm-time trough on April 20, 1985, *Journal of Atmospheric and Solar-Terrestrial Physics*, *65*(2), 211–217. https://doi.org/10.1016/S1364-6826(02)00292-4

Xu, H., Shiokawa, K., Oyama, S. I., & Otsuka, Y. (2019). Thermospheric wind variations observed by a Fabry-Perot interferometer at Tromsø, Norway, at substorm onsets. *Earth, Planets and Space*, *71*(1), 93. https://doi.org/10.1186/s40623-019-1072-0

Young, R. A. (1969), Chemiluminescent reactions in the airglow, *Canadian Journal of Physics*, *47*(10), 1927–1937.

Zhang, Y., Paxton, L. J., Morrison, D., Marsh, D., & Kil, H. (2014). Storm-time behaviors of O/N_2 and NO variations. *Journal of Atmospheric and Solar-Terrestrial Physics*, *114*, 42–49. https://doi.org/10.1016/j.jastp.2014.04.003

Zipf, E. C., Borst, W. L., & Donahue, T. M. (1970). A mass spectrometer observation of NO in an auroral arc. *Journal of Geophysical Research*, *75*(31), 6371–6376. https://doi.org/10.1029/JA075i031p06371

Zou, S., Lyons, L. R., & Nishimura, Y. (2012). Mutual evolution of aurora and ionospheric electrodynamic features near the Harang reversal during substorms. *Geophysical Monograph Series*, *197*, 159–169. https://doi.org/10.1029/2011GM001163

Zou, S., Lyons, L. R., Wang, C.-P., Boudouridis, A., Ruohoniemi, J. M., Anderson, P. C., et al. (2009). On the coupling between the Harang reversal evolution and substorm dynamics: A synthesis of SuperDARN, DMSP, and IMAGE observations. *Journal of Geophysical Research*, *114*(A1), A01205. https://doi.org/10.1029/2008JA013449

Zou, Y., Lyons, L., Conde, M., Varney, R., Angelopoulos, V., & Mende, S. (2020). Effects of Substorms on High-Latitude Upper Thermospheric Winds. *Journal of Geophysical Research: Space Physics*, *126*(1), e2020JA028193. https://doi.org/10.1029/2020JA028193

Zou, Y., Nishimura, Y., Lyons, L., Conde, M., Varney, R., Angelopoulos, V., & Mende, S. (2018). Mesoscale *F* region neutral winds associated with quasi-steady and transient nightside auroral forms. *Journal of Geophysical Research: Space Physics*, *123*(9), 7968–7984. https://doi.org/10.1029/2018JA025457

References From the Supporting Information

Donovan, E., Spanswick, E., Liang, J., Grant, J., Jackel, B., & Greffen, M. (2012). Magnetospheric dynamics and the proton aurora. In A. Keiling, E. Donovan, F. Bagenal, T. Karlsson (Eds.), *Auroral Phenomenology and Magnetospheric Processes: Earth and Other Planets* (pp. 365–378). Washington, DC: AGU.

Immel, T. J., Mende, S. B., Frey, H. U., Peticolas, L. M., Carlson, C. W., Gerard, J. C., et al. (2002). Precipitation of auroral protons in detached arcs, *Geophysical Research Letters*, *29*(11), 14-1–14-4. https://doi.org/10.1029/2001GL013847

Lyons, L. R., Nishimura, Y., Gallardo-Lacourt, B., Nicolls, M. J., Chen, S., Hampton, D. L., et al. (2015). Azimuthal flow bursts in the inner plasma sheet and possible connection with SAPS and plasma sheet earthward flow bursts. *Journal of Geophysical Research: Space Physics*, *120*(6), 5009–5021. https://doi.org/10.1002/2015JA021023

Nishimura, Y., Bortnik, J., Li, W., Lyons, L. R., Donovan, E. F., Angelopoulos, V., & Mende, S. B. (2014). Evolution of nightside subauroral proton aurora caused by transient plasma sheet flows. *Journal of Geophysical Research: Space Physics*, *119*(7), 5295–5304. https://doi.org/10.1002/2014JA020029

Wallis, D. D., Burrows, J. R., Moshupi, M. C., Anger, C. D., & Murphree, J. S. (1979). Observations of particles precipitating into detached arcs and patches equatorward of the auroral oval, *Journal of Geophysical Research*, *84*(A4), 1347–1360. https://doi.org/10.1029/JA084iA04p01347

Zhang, Y., Paxton, L. J., Morrison, D., Wolven, B., Kil, H., & Wing, S. (2005), Nightside detached auroras due to precipitating protons/ions during intense magnetic storms, *Journal of Geophysical Research*, *110*(A2), A02206. https://doi.org/10.1029/2004JA010498